THE PENNSYLVANIA STATE UNIVERSITY
SCHREYER HONORS COLLEGE

DEPARTMENT OF PHYSICS

PROGRESS TOWARDS A MEASUREMENT OF THE ELECTRON ELECTRIC DIPOLE MOMENT USING COLD CS AND RB ATOMS IN A 1D OPTICAL TRAP

MATTHEW FITZGERALD EBERT
Spring 2010

A thesis
submitted in partial fulfillment
of the requirements
for baccalaureate degrees
in Physics and Mathematics
with honors in Physics

Reviewed and approved* by the following:

David S. Weiss
Professor of Physics
Thesis Supervisor

Richard W. Robinett
Professor of Physics
Honors Advisor

* Signatures are on file in the Schreyer Honors College.

Abstract

In this thesis, we report progress towards a measurement of a permanent electric dipole moment (EDM) of cold Cesium and Rubidium atoms in a 1D optical lattice. A stable particle cannot have an EDM unless time-reversal and parity symmetry are violated. The Standard Model predicts an electron EDM of about 10^{-38} e-cm, which is far smaller than the current experimental limit of 1.6×10^{-27} e-cm. Much larger EDMs are predicted by proposed extensions to the Standard Model, such as Supersymmetry, Multi-Higgs and Left-Right symmetric models. Therefore, the detection of an EDM in the current experimental range would be the first direct observation of time-reversal symmetry breaking, and the first experimental observation of any kind that is inconsistent with the Standard Model.

Laser cooling and trapping of atoms in precision measurements greatly reduces noise sources and increases the sensitivity of the experiment. Both Cesium and Rubidium are used, because laser trapping techniques for Cs and Rb atoms are well understood and because of the large EDM enhancement factors for each. The projected sensitivity of our experiment is 3×10^{-30} e-cm, a 500-fold improvement over the current experimental limit and sensitive enough to test proposed extensions to the Standard Model. If a non-zero EDM is detected, the two species will provide a strong final check against systematic errors.

The sensitivity of the experiment is determined by a few factors, one of which is magnetic field gradients, which in combination with an electric field gradient and imperfect electric field reversal can produce a false EDM signal. To reduce the magnetic gradient, two levels of cancellation coils and a magnetic shield will be implemented. Surrounding the experiment are six sets of background magnetic field cancellation coils that reduce the magnetic field to the mG range in order to prevent saturation of the shields due to the Earth's magnetic field. Surrounding the cavity where the atoms will be trapped is a passive shield constructed of μ-metal, which will decrease the magnetic field inside by a factor of at least 10^{-4}. Inside the shield there will be eight sets of magnetic coils designed to produce highly uniform magnetic bias fields and magnetic gradients. The spatial uniformity of the fields and field gradients are determined by the geometry of the coils, while the accuracy, precision, noise, and any time dependent effects are dictated by the power supply.

The development and integration of a computer-controlled, low-noise, accurate power supply system for the coils will be discussed, as well as an introductory overview of the experiment and sources of error. An exhaustive description of the experiment is beyond the scope of this thesis.

Acknowledgments

I am grateful to my friends and family for their unfaltering support. I would also like to thank Neal Meyer and Kunyan Zhu for their constant guidance, helpful conversations, and willingness to share the two lab computers. Finally I would like to acknowledge my advisor, Prof. David Weiss, for his patience and insightful talks.

Table of Contents

List of Tables

List of Figures

Chapter 1

Introduction

The motivation for this work is to search for a permanent atomic electric dipole moment (EDM) of Cesium and Rubidium atoms. A permanent EDM is the property of a particle to experience a linear shift in energy, U, when influenced by an external electric field, as seen in Equation 1.1. The EDM of an atom, d_a, is related to the electron EDM, d_e and will be discussed in Section 1.1.3.

$$U = -\mathbf{d_a} \cdot \mathbf{E}. \tag{1.1}$$

Experiments to detect an EDM began in 1950 with Ramsey and Purcell using a polarized neutron-beam magnetic resonance apparatus [1]. Using this technique a limit of 5×10^{-20} e-cm was placed on the neutron EDM [2]. Over the years there have been improvements of many orders of magnitude in the limits on the nuclear and electron EDM. Modern experimental techniques, such as laser cooling and trapping of atoms, can be used to increase sensitivity and decrease noise in precision measurements. A chart depicting the sensitivity of EDM experiments over time is provided in Figure 1.1. In this thesis, I will report on our progress towards the measurement of an EDM using cold Cs and Rb atoms in a 1D optical lattice.

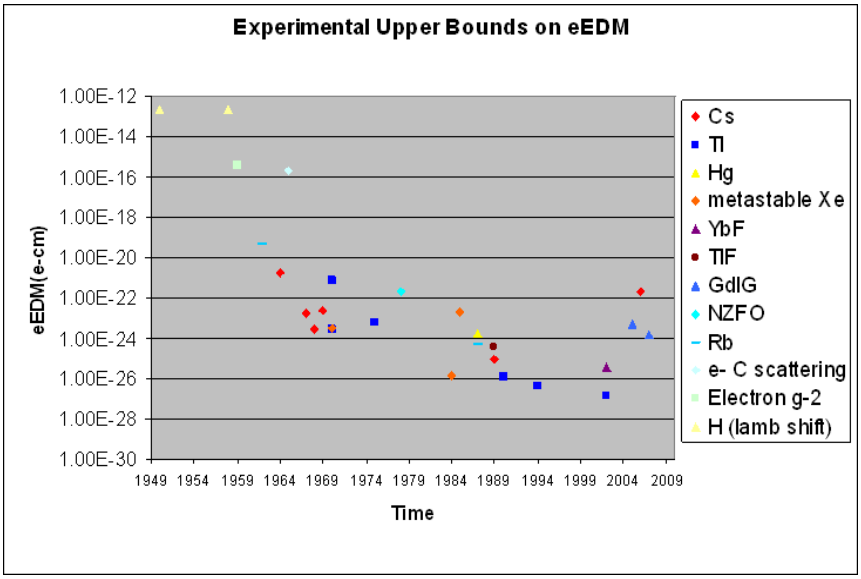

Fig. 1.1. Experimental upper bounds on the electron EDM from various experiments over time. The more recent limits are the first results of newer experiments which have not yet reached their projected sensitivity.

1.1 EDM Theory

1.1.1 Fundamental Symmetries

The existence of a permanent EDM of a stable particle implies a violation of time-reversal (T) and parity-reflection (P) symmetries. This is because the expectation value of the EDM operator is proportional and parallel to the spin of the electron (or the total angular momentum), see Equation 1.2 where d is the electron EDM and s is the spin of the electron. The EDM must be parallel to the spin. If not, additional EDM "up" and "down" states would exist in atomic structure, thus doubling the electrons which could inhabit an atomic shell due to the Pauli Exclusion Principle, a phenomenon which is not observed [3].

$$\mathbf{d} = d\frac{\mathbf{s}}{s}. \tag{1.2}$$

T symmetry violation arises from the fact that d is odd and s is even under T, and similarly P symmetry violation is due to the fact that d is even and s is odd under P (see Figure 1.2) [4]. If d is zero, then there is, of course, no symmetry violation, but a non-zero EDM requires P and T violation, by virtue of Equation 1.2.

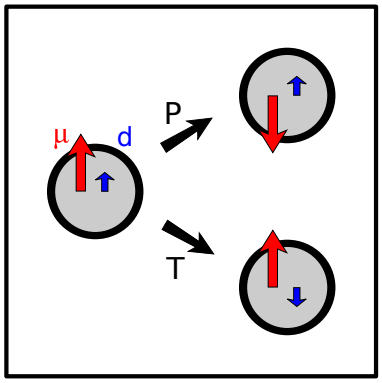

Fig. 1.2. Transformations of the electron EDM under T and P reversals. Each produces a different state with μ and d anti-parallel

The CPT theorem states that the combined charge conjugation (C), parity reflection (P), and time-reversal (T) symmetries are invariant. Because the proof of this theorem follows directly from general assumptions such as Lorentz-invariance and locality, there are strong reasons to expect the CPT theorem and no experimental reasons yet to doubt it [5]. However, in general there is no such theorem requiring the individual symmetries (C, P and T) to be invariant. This means that if an individual symmetry or a combination of symmetries is broken, then under the CPT theorem at least one of the remaining symmetries must also be broken to maintain CPT invariance.

Prior to the 1950s, Parity conservation was considered by most to be beyond any doubt. However, the first symmetry violation to be observed was P violation in ^{60}Co

β decay suggested by Yang and Lee [6] and observed by Wu in 1957 [7]. A second example of symmetry violation can be deduced from the fact that under C left-handed neutrinos become left-handed anti-neutrinos, but all observed neutrinos are left-handed and all observed anti-neutrinos are right-handed [8]. Finally the combined charge and parity symmetry (CP) violation was observed in 1964 due to K^0 meson decay. The origin of this symmetry violation is not known but the standard model can account for it phenomenologically. According to the CPT theorem, the CP violation implies a T asymmetry [9], although as of yet there has not been any direct observation of T symmetry breaking. In effect, the search for an EDM is also a search for T violation or equivalently CP violation. From now on, the terms T and CP invariance will be used interchangeably.

1.1.2 Physics beyond the Standard Model

According to the CPT theorem, the combined CPT symmetry is conserved in any Lorentz-invariant local quantum field theory, including the Standard Model [5]. The Standard Model predicts a non-zero electron EDM, the magnitude of which is expected to be about 10^{-38} e-cm, determined using a simple power counting argument [4]. The value is so small due to a cancellation of the leading order Feynman diagrams [10]. This value is more than ten orders of magnitude smaller than the current experimental limit of 1.6×10^{-27} e-cm, observed in ^{205}Tl [11]. However, several proposed extensions to the Standard Model predict new T violating interactions, and as a consequence predict much larger EDMs on the order of the current experimental limit, see Figure 1.3 for a list of these ranges.

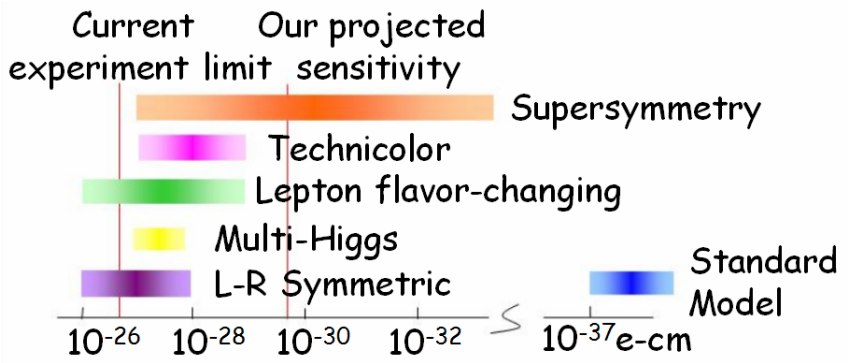

Fig. 1.3. Predicted electron EDM Ranges for various models

The detection of an EDM at the current observable level would be, in addition to the first direct observation of T violation, unambiguous evidence for physics beyond the Standard Model. Additionally, if an EDM is not detected in the next few orders of magnitude, considerable constraints would be placed on a number of models. A number of models have already been ruled out or constrained by the increasing sensitivity of EDM measurements over the years, including Weinberg's 3-Higgs model that attempted to explain the source of K^0 meson and neutron T violation [3]. In addition, the detection of a neutron EDM near the current experimental limit but no electron EDM could imply that the EDM has a QCD origin [12].

1.1.3 The Schiff Theorem

When measuring the atomic EDM of an atom, it is interesting to consider the Schiff Theorem. The Schiff Theorem states that there can be no atomic EDM arising from the contribution of the constituent particles due to shielding by the other constituent

particles under certain conditions [13]. In order for Schiff's model to hold the following conditions must be met:

- Atoms consist of non-relativistic particles
- The constituent particles only interact electrostatically
- The EDM distribution of each atomic constituent is identical to its charge distribution.

According to the model, there is no effect on the atomic EDM from the constituent particles, because under an applied electric field the electron cloud will rearrange itself to cancel any effect of an electron or neutron EDM [13]. However, in reality these assumptions are violated by the fact that the electron is a relativistic particle and the spin-orbit interaction. Therefore, the Schiff model does not hold. In fact in heavy atoms, where the electron velocity is relativistic in the inner shells, Schiff's non-relativistic approximation breaks down completely and there is actually an enhancement of the electron EDM, d_e, in the atomic EDM, d_a [4].

1.1.4 The Enhancement Factor

In this experiment, we will attempt to detect an atomic EDM using Cs and Rb atoms. There are multiple benefits to using paramagnetic atoms in an electron EDM search, not the least of which is that a free electron would be accelerated in an electric field during any attempts to measure an EDM. Measuring an atomic EDM of a neutral atom is a favorable approach, but an atomic EDM need not originate solely from an electron EDM. There are four possible mechanisms listed below that could create one [4]:

- An electron EDM
- A nuclear EDM
- T-violating quark-quark interactions
- T-violating electron-nuclear interactions

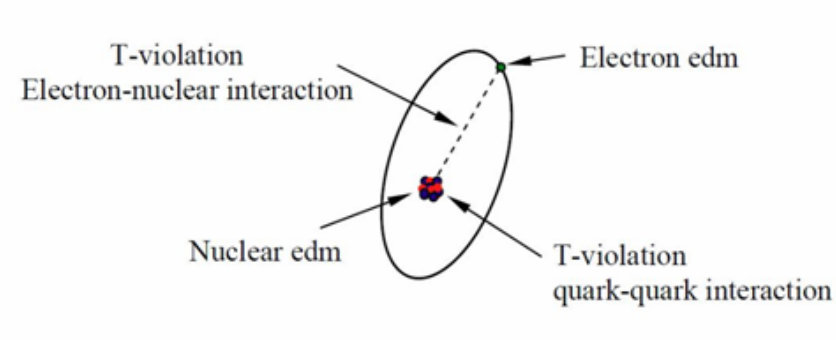

Fig. 1.4. T-violating processes that could give rise to an atomic EDM, from reference [14]

Despite the four possible causes for atomic EDMs, paramagnetic atoms are not affected by nuclear EDMs or quark-quark interactions because the Schiff theorem is valid for the nucleus, implying a nuclear EDM would be completely shielded [5]. In addition, heavy paramagnetic atoms have an EDM enhancement factor that increases the magnitude of the atomic EDM proportional to the electron EDM. This enhancement factor R is approximately given by Equation 1.3, where Z is the atomic number and α is the fine structure constant [3].

$$R = \frac{d_a}{d_e)} \propto \alpha^2 Z^3. \tag{1.3}$$

The enhancement factor R increases as the cube of the atomic number. This means the atomic EDM becomes increasingly large with heavier atoms, making these atoms a more sensitive probe for the electron EDM. The enhancement factors for Cs and Rb are 125.9 and 24.6 respectively, for enhancement factors of other atoms and molecules commonly used in EDM searches see Table 1.1.

Atom/Molecule	Rb	Cs	Tl	Fr	PbO
R	24.6	125.9	585	1150	≈60000

Table 1.1. Enhancement factors for atoms and molecules commonly used in EDM measurements [11, 15, 16]

Although Cs and Rb tend to be on the smaller end of the listed enhancement factors, we use them in our experiment because the laser cooling and trapping techniques for Cs and Rb are more mature. These species can be easily cooled to low temperatures enabling longer integration times, increasing sensitivity and decreasing measurement noise. Additionally, the underlying atomic theory for alkali atoms is very precise with an error of $< 1\%$ [16, 17], making alkali atoms a more precise measure of the fundamental symmetries if an EDM is detected.

1.2 Previous EDM Experiments

The change in potential energy of an EDM in an electric field is linear, see Equation 1.1, so a larger electric field will create a larger change in potential energy. A typical experiment involves performing a differential measurement of the potential energy with the electric field parallel to the spin of the sample, and the terms $-\mu \cdot \mathbf{B}$ and $-\mathbf{d} \cdot \mathbf{E}$ are

added to the Hamiltonian. If the experiment is repeated with the electric field direction reversed, the terms added to the Hamiltonian become $-\mu \cdot \mathbf{B}$ and $\mathbf{d} \cdot \mathbf{E}$. This simple differential measurement technique allows the experiment to be insensitive to constant magnetic fields that are homogeneous over the sample. More sophisticated techniques may also be incorporated to further reduce sensitivity to magnetic fields.

1.2.1 Neutron EDM Experiments

The current experimental limit on the neutron EDM is 6.3×10^{-26} e-cm and was performed by using ultra cold neutrons in a resonance spectrometer [18, 19]. The neutron spin polarization precesses at the Larmor frequency which was measured in parallel and anti-parallel electric fields. Since the Larmor frequency depends on the potential energy of the neutron, the presence of an EDM would change the frequency slightly. In order to correct for fluctuations in the magnetic field which significantly hampered early results, an internal "comagnetometer" of polarized ^{199}Hg atoms was added in the same cell as the neutrons. The necessary addition of this comagnetometer demonstrates the degree to which magnetic field fluctuations can have an effect on an EDM experiment.

1.2.2 Atomic EDM Experiments

There are two types of atoms used in atomic EDM searches, paramagnetic and diamagnetic. Paramagnetic atoms (Cs, Rb, Tl, Fr) are sensitive to the electron EDM, see Section 1.1.3. The highest sensitivity to the electron EDM has been obtained with paramagnetic atoms, and is $d_e < 1.6 \times 10^{-27}$e-cm [11]. The result was obtained by the Commins group with hot Tl beams, where sodium atoms served as a comagnetometer to

improve the sensitivity of the experiment. The Tl atoms were prepared in the $m_F = 0$ state and then transferred to a superposition of the $m_F = \pm 1$ states. After the atoms passed through an electric field region, another RF pulse was applied. The number of atoms that returned back to the $m_F = 0$ state is related to the size of the EDM signal.

Diamagnetic atoms (Hg, Xe, Rn), with closed electron shells, have enhancement factors less than one, but the sensitivity of diamagnetic atom experiments to the atomic EDM make them competitively sensitive to underlying EDMs, most notably to nuclear EDMs [20, 21]. The Fortson group has placed an experimental limit of 3.1×10^{-29}e-cm on the atomic EDM of ^{199}Hg. The experiment used hot ^{199}Hg atoms in a stack of four vapor cells with a common magnetic field and oppositely directed electric fields. This design makes the experiment insensitive to time varying magnetic fields that are homogeneous over the cells. To measure the EDM, the Zeeman procession frequency of the nuclear spin of ^{199}Hg atoms is determined by measuring the polarization change of a probe laser perpendicular to the precession axis [22, 20].

1.2.3 Molecular EDM Experiments

EDM searches in molecules (YbF, PbO, TlF) take advantage of large EDM enhancement factors. Large internal effective electric fields in heavy diatomic polar molecules are due to strong polarization along the internuclear axis [23]. As long as an electric field is applied to the molecules which prevents rotations, the strong internal field will not average to zero. The effective internal electric field (E_{eff}) of YbF can be up to 26 GV/cm. A first result using YbF molecules reached a sensitivity of $(-0.2 \pm 3.2) \times 10^{-26}$e-cm [23].

1.2.4 Solid State EDM Experiments

Solid state EDM experiments benefit from large signals but systematic errors are more difficult to understand and control. If a strong electric field is applied to a compound containing unpaired electron spins, the electron EDMs should align with the field and the magnetic field could be measured [24]. This method was attempted in 1978 with nickel-zinc ferrite, but was unable to produce useful results due to experimental limitations such as high sample conductivity, high operating temperature, and limited SQUID technology [25]. Alternatively, the electrons could be polarized with a magnetic field that would also polarize the EDMs by virtue of Equation 1.2, causing a voltage across the sample [26].

1.3 Overview of Experimental Method

A broad overview of the experimental method is as follows. We will load the atoms (Cs or Rb, not both) into a magneto-optical trap (MOT) which can overlap either of the two 1D optical lattices. The atoms will then be launched approximately 90 cm into a magnetically shielded region above the MOT and recooled in the lattices using a separate set of optical molasses beams. The lattices are located between a stack of three transparent electric field plates, with one plate shared. When the plates are charged, the atoms in either lattice will experience electric fields that are equal in magnitude and opposite in direction. When the lattices are fully loaded, approximately 200 spatially distinct groups of atoms can be individually addressed, which can provide information concerning residual magnetic fields and systematic errors. During the measurement,

the electric field will serve as the quantization axis for Ramsey-like spectroscopy among ground state sublevels that are sensitive to the atomic EDM. Using cold trapped atoms increases the coherence time and significantly reduces motional errors such as $\mathbf{v} \times \mathbf{E}$ effects, but trapping lasers introduce other potential systematic errors.

Chapter 2

General Features of EDM Experiment

In our experiment, we will trap Cs and Rb atoms in two, 10 cm long, 1D optical lattices, in alternating measurements. Because the atomic EDMs of Cs and Rb are predicted to differ by a factor of 5.1[16], if an EDM is detected our unique two species design will provide a strong final check against systematic errors. With a 12 hour integration time, the sensitivity of the experiment is projected to be 3.0×10^{-30} e-cm. In this chapter, the experimental method is discussed. A schematic of the experiment is shown in Figure 2.1.

2.1 Atom Processing

One atomic species (Cs or Rb) will be loaded at a time from an atomic beam oven. The atomic beam will be slowed using a Zeeman slower and then trapped in a magneto-optical trap (MOT) [27]. The MOT center can be shifted 5 mm to overlap with either the $+z$ or $-z$ 1D optical lattice. The MOT is filled, at which point the trapped atoms are launched up, guided by one of the two lattices. While the atoms are in transit, we begin refilling the MOT for the next launch.

To launch the loaded MOT, a frequency difference is imposed on the optical molasses laser beams, effectively creating a moving reference frame and launching the atoms 1 m high into a magnetically shielded region sufficiently distant from the MOT

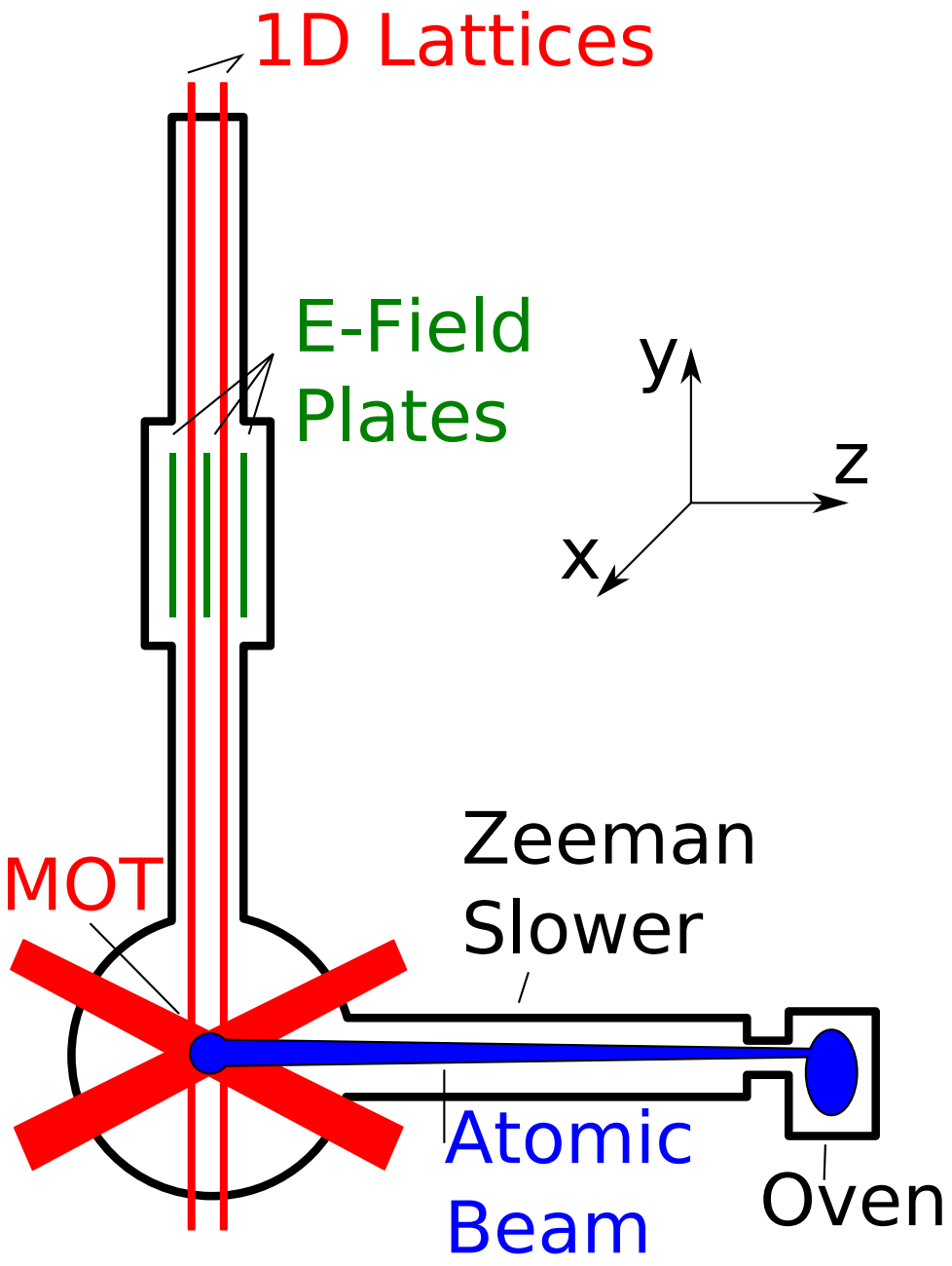

Fig. 2.1. Simplified schematic of the experiment. The an atomic beam of Cs or Rb is cooled in a Zeeman slower and collected in a MOT, which overlaps the two lattices. The atoms are then launched up the lattices and retrapped in the measurement region between the stack of 3 electric field plates. The inset is an image of the actual electric field plates. A more detailed sketch of the electric field plates is shown in Figure 2.1.

(see Chapter 3 for information regarding magnetic fields). During the launch, the atoms are guided by the lattice's time averaged transverse dipole force [28]. The atoms are retrapped, using separate optical molasses beams, about 10 cm before the top of their trajectory. The atoms are trapped in 2 cm tall stack of "pancake" shaped traps, see Figure 2.2. Performing multiple loads and launches to various heights over approximately 1 second can create 10 cm tall stacks in each lattice containing $\approx 10^8$ or $\approx 4 \times 10^9$ Cs or Rb atoms respectively [14].

Each lattice is situated between two transparent 30×5 cm electric field plates, one of which is shared, to enable simultaneous measurement of the atoms in either of two oppositely directed electric fields, see Figure 2.2. The symmetric design allows for cancellation of noise common to both lattices. The plates are coated with Indium Tin Oxide (ITO), which is transparent and makes the plates conductive. Additionally, the outer plates have an anti-reflection coating, while the inner plate has a high-reflection coating. The electric fields produced by these plates define the quantization axis of the experiment. After the traps have been loaded and cooled, the atoms are optically pumped to the stretched magnetic sublevels $m_F = \pm F$ and then brought to the $m_F = 0$ sublevel by a series of adiabatic fast passage microwave pulses. The lattice depth is then lowered and the plates are charged to up to 150 kV/cm in approximately 0.5 sec [14].

2.2 EDM Measurement

The measurement procedure begins by driving the atoms, originally in the $m_F = 0$ state, into a superposition of the $m_F = \pm 3$ states by applying a low-frequency transverse magnetic field. The atoms experience 3 seconds of coherent free evolution. During

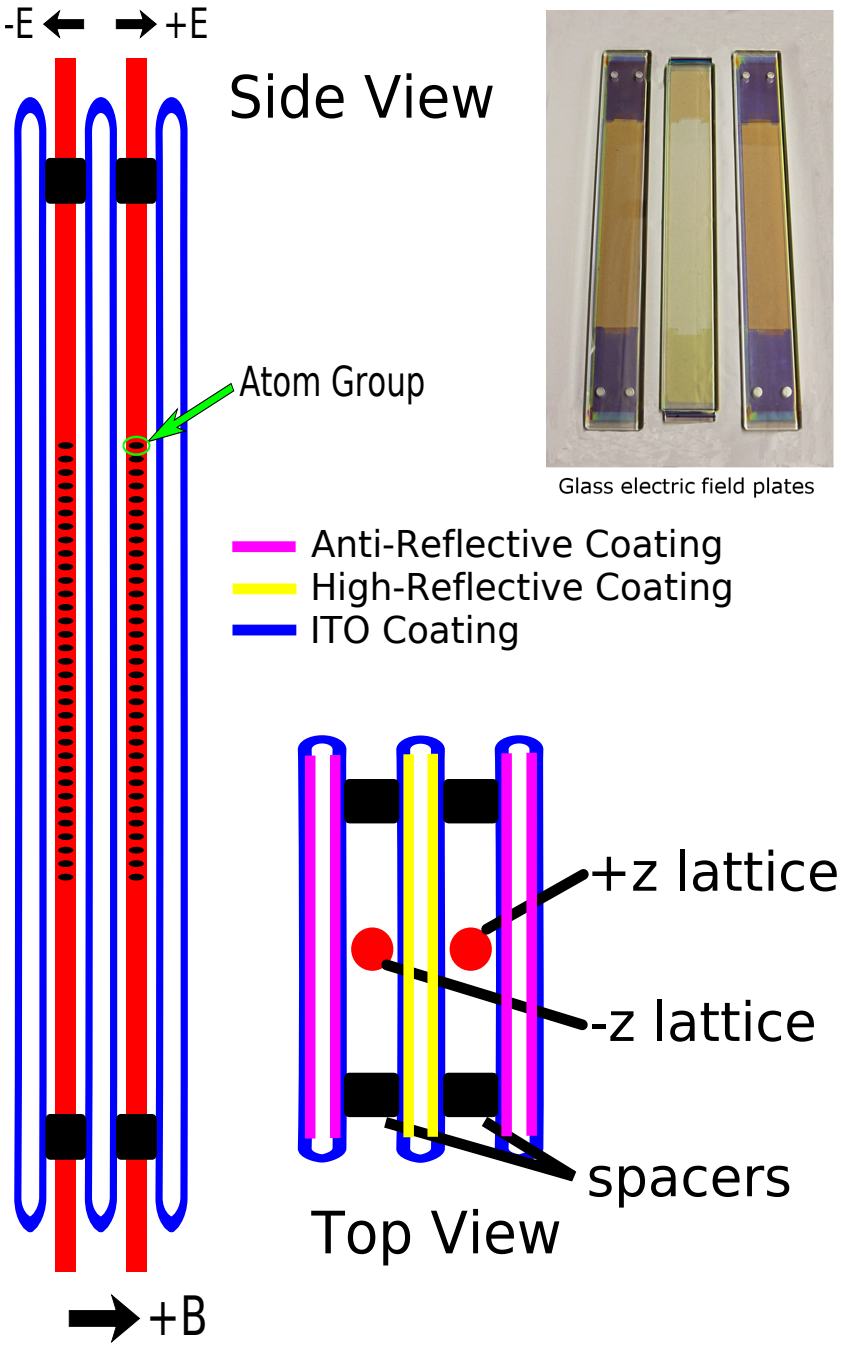

Fig. 2.2. Sketch of the electric field plates with atoms trapped in two 10 cm high 1-D lattices. Each lattice is situated between two transparent electric field plates, with the center plate shared and charged to 60 kV.

this time, the relative phase between the $m_F = \pm 3$ states evolves. After the coherent evolution, the atoms will be returned to the $m_F = 0$ state. The population of atoms returning to the $m_F = 0$ is sensitive to the energy difference between the stretched states. This procedure is similar to that of the previous Thallium atomic beam experiments.[11] The electric field is turned off and the atoms in the $F = 3$ ground states are transfered to the $F = 4$ state by a microwave transition. The populations are determined from the intensity of the fluorescence on the $F = 4$ to $F' = 5$ cycling transition. The fluorescence from ≈ 200 individual groups will be detected using Fresnel optics and a linear CCD array. The measurement will then be repeated with the electric fields reversed. The proportion of atoms returning to the ground state is given by Equation 2.1, where $\frac{n}{n_0}$ is the ratio of atoms returning to the $m_F = 0$ state and τ is the time spent in the coherent free evolution. An example of the EDM signal described is shown in Figure 2.3.

$$\frac{n}{n_0} = Cos^2(\frac{\mu B + dE}{\hbar}\tau). \tag{2.1}$$

A non-zero EDM implies that the energy splitting between two stretched states is different depending on whether the direction of the electric field. An energy level diagram of the atoms during the coherent evolution is shown in Figure 2.4. The EDM signal will be obtained by a differential measurement of the phase difference due to this energy shift in oppositely directed electric fields. This is performed for each pair of groups in the stacks and averaged over a 12 hour integration time. The phase difference obtained during the coherent evolution is given by $\phi_1 - \phi_2$. If the phase difference obtained due to

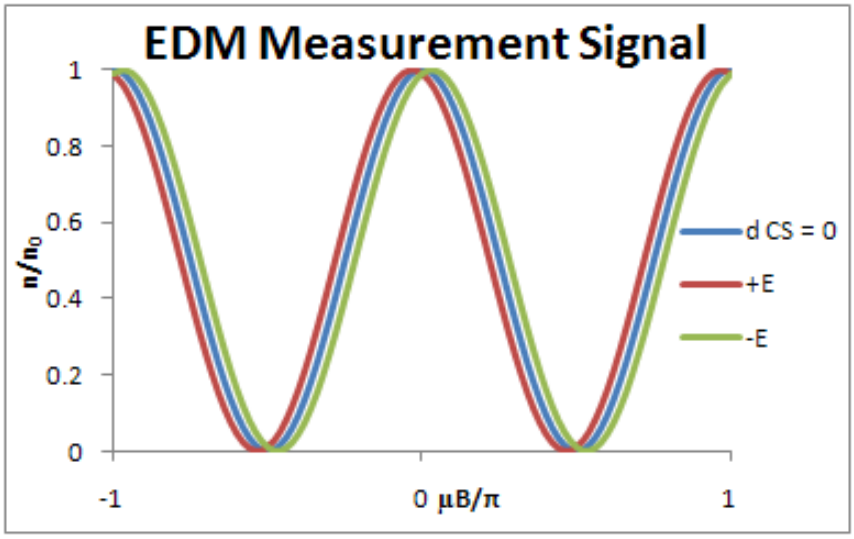

Fig. 2.3. The EDM signal in oppositely directed electric fields

the electric field reversal is included, the EDM signal is then described by Equation 2.2, where ϕ^+ and ϕ^- are the phase differences during the original electric field orientation and electric field reversal respectively.

$$\frac{4Ed_a}{\hbar}\tau = (\phi_1^+ - \phi_2^+) - (\phi_1^- - \phi_2^-). \tag{2.2}$$

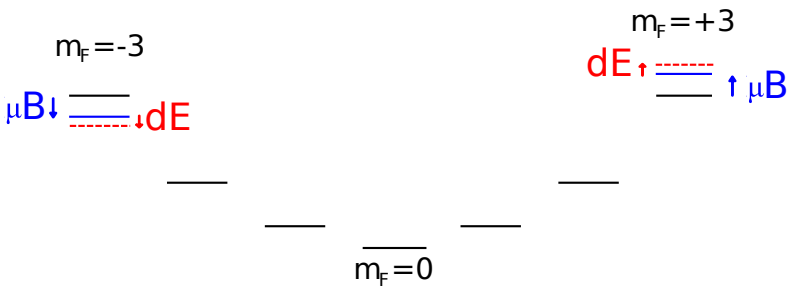

Fig. 2.4. Energy level diagram for atoms during coherent evolution assuming positive electric and magnetic field orientations. The separation between the m_F =0 and ±3 states is ≈ 400 Hz and the splitting due to a 500 nG magnetic field is ≈0.5 Hz.

Chapter 3

Magnetic Field Sensitivity, Noise, and Error Analysis

In this chapter the effect of magnetic field noise and gradients on the EDM measurement is discussed. For a comprehensive discussion of noise and error sources see reference [14].

3.1 Sensitivity

Because the EDM is so small, a direct measurement of the frequency shift in an electric field is not possible and the differential measurement method described in Section 2.2 is necessary. Since the differential measurements are performed simultaneously noise that is common mode to both lattices can be canceled. The EDM signal is detected from a shift in the Ramsey fringe dependent on the sign and magnitude of the electric field (see Figure 2.3). Magnetic field noise will cause variations in the energy levels of the stretched states during the coherent evolution. This implies that the experiment is sensitive to magnetic field noise that is not common-mode. The derivation of the magnetic field sensitivity was originally discussed in reference [14] and is reproduced here. The magnetic field experienced by the atoms can be described by Equation 3.1.

$$B(z,t) = B_0 \pm \Delta B_z \pm \Delta B_t \pm \Delta B_{zt}. \tag{3.1}$$

Where B_0 is the constant bias field, ΔB_z is the magnetic field gradient between groups experiencing opposite electric fields, ΔB_t is the common-mode noise between the two groups, and ΔB_{zt} are the fluctuations of the magnetic field associated with both space and time. Using Equations 2.1 and 3.1, the phase delay, ϕ, experienced by a group can be described by Equations 3.2-3.5.

$$\phi_1^+ = \frac{\mu(B_0 + \Delta B_z + \Delta B_t + \Delta B_{zt}) + dE}{\hbar}\tau \tag{3.2}$$

$$\phi_2^+ = \frac{\mu(B_0 - \Delta B_z + \Delta B_t - \Delta B_{zt}) - dE}{\hbar}\tau \tag{3.3}$$

$$\phi_1^- = \frac{\mu(B_0 + \Delta B_z - \Delta B_t - \Delta B_{zt}) - dE}{\hbar}\tau \tag{3.4}$$

$$\phi_2^- = \frac{\mu(B_0 - \Delta B_z - \Delta B_t + \Delta B_{z,t}) + dE}{\hbar}\tau. \tag{3.5}$$

Here the subscript denotes the spatial group where 1 and 2 correspond to the '+' and '-' z groups respectively, and the superscript refers to whether the electric field is reversed or not. Therefore by Equation 2.2, the EDM signal including the error is calculated with Equation 3.6.

$$\frac{4Ed_a}{\hbar}\tau + 4\Delta B_{zt} = (\phi_1^+ - \phi_2^+) - (\phi_1^- - \phi_2^-). \tag{3.6}$$

From Equation 3.6, it is apparent that the EDM signal is sensitive to temporal fluctuations in magnetic field gradients, but insensitive to common-mode magnetic field noise and time independent gradients (a static magnetic field gradient effect will be discussed in Section 3.3). Time dependent magnetic field gradients must be kept at a minimum,

preferably below the shot noise limits listed in Equations 3.7-3.8 [14].

$$\frac{\delta\omega_{Cs}}{2\pi} = \frac{1}{\sqrt{NT\tau}} \sim 3 \times 10^{-7} Hz \tag{3.7}$$

$$\frac{\delta\omega_{Rb}}{2\pi} = \frac{1}{\sqrt{NT\tau}} \sim 0.7 \times 10^{-7} Hz. \tag{3.8}$$

The smallest magnitude magnetic field noise and gradients is always preferable for maximum sensitivity.

The sensitivity of measuring N uncorrelated atoms is limited by the shot noise or Poisson distribution, $\sqrt{N}$, due to quantum statistics. In order to achieve the shot noise limit in the sensitivity of measurement, all noise and error sources must be below the shot noise limit. Uncorrelated noise can be averaged out by increasing the integration time. However, systematic errors are errors that affect the energy difference between the stretched states differently depending on the direction of the electric field. Unlike noise errors, systematic errors cannot be averaged out, and will cause an offset in the signal mimicking an EDM. Therefore systematic errors must be less than the EDM signal which we hope to measure. With an integration time T of 12 hours, an electric field of 150 kV/cm, a coherence time of 3 seconds, and 10^8 and 2×10^9 atoms for Cs and Rb respectively, the experimental sensitivity is obtained by Equation 3.9.

$$\left\langle \delta d_e \right\rangle = \frac{\hbar}{4RE\sqrt{NT\tau/2}}. \tag{3.9}$$

Using the parameters listed above a sensitivity of approximately 3×10^{-30} e-cm can be achieved. To increase the sensitivity, more atoms, a larger electric field, or a longer integration time is required.

3.2 Statistical Noise

Statistical noise is noise which is not correlated with the direction of the electric field and can therefore be averaged out by increasing the number of runs. Effects which are correlated with the direction of the electric field and will mimic an EDM signal are referred to as systematic errors, and need to be kept below the projected sensitivity of the experiment, see Section 3.3. This experiment is not sensitive to noise which is common-mode to both lattices, because it is sensitive only to the phase difference between the two groups of atoms. In this section statistical noise due to magnetic field fluctuations is discussed.

There are two sources of time dependent magnetic field fluctuations. The first is environmental fluctuations as a result of imperfect magnetic field shielding. The second is magnetic fields induced by Johnson Noise in the magnetic shielding, the ITO coating on the electric field plates, and various Titanium components located inside the magnetic shielding.

3.2.1 Johnson Noise

Johnson (or Nyquist) noise is current noise associated with thermal motion of electrons in bulk conductors at equilibrium. This current noise gives rise to a magnetic field noise. A static approximation of the currents in a conductor (i.e. eddy currents

are ignored) can be made when the thickness of the conductor is less than the skin depth, which for μ-metal is approximately 1 mm at 1 Hz [29]. Since eddy currents in thicker conductors effectively shield the internal currents fluctuations a reasonable upper bound on magnetic field noise can be imposed with a simple calculation using the static approximation. The magnetic field at an arbitrary point outside the surface of the conductor can be found by the Biot-Savart law using the current density inside the conductor given by Equation 3.10.

$$i_{rms} = \sqrt{4k_B T \sigma \delta f}. \tag{3.10}$$

Here k_B is Boltzmann's constant, T is the temperature, and σ is the conductivity. Using Equation 3.10 an upper bound on the magnetic field noise from a rectangular block of thickness t located a distance l from the point of interest is derived from the Biot-Savart law, and is given by Equation 3.11.

$$B_{block} = \frac{\mu_0}{2\pi}\sqrt{k_B \sigma T}\int_{-\Delta x/2}^{\Delta x/2}\int_{-\Delta y/2}^{\Delta y/2}\int_{l}^{l+t}\sqrt{\frac{x^2+y^2}{(x^2+y^2+z^2)^3}}dzdydx. \tag{3.11}$$

Where the x, y dimensions of the block are given by Δx and Δy. Johnson noise from multiple sources is uncorrelated and therefore is added in quadrature. Because the mirror mounts are located about 30 cm away from the atoms, the magnetic field Johnson noise is common mode and mostly gets canceled. For one Ti mirror mount the magnetic field Johnson noise is 10.5 pG/$\sqrt{Hz}$ and for 4 mirror mounts it is 14.8 pG/$\sqrt{Hz}$. One of these mirror mounts is shown in Figure 3.1.

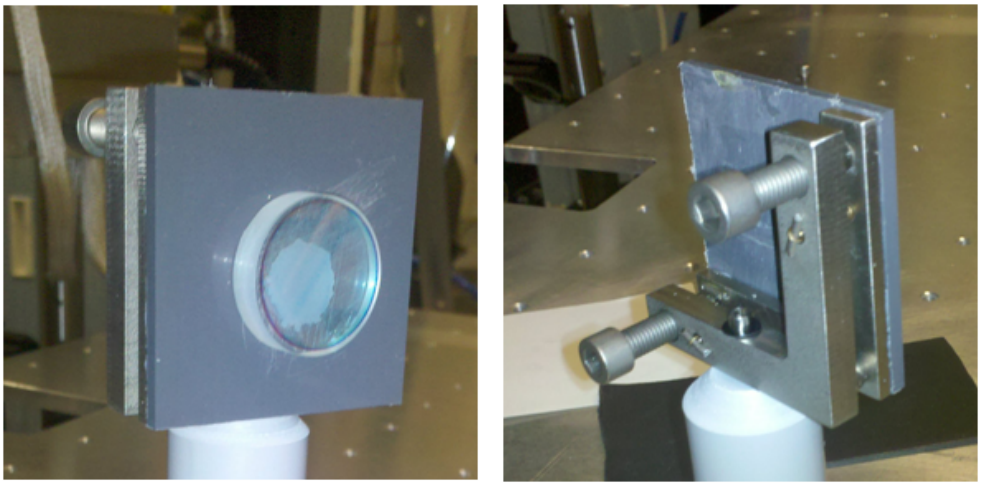

Fig. 3.1. A custom Ti mirror mount is shown. The back piece is two "L" shaped Ti pieces with 2 inch sides. The front is a 2×2 inch piece of plastic. The mirror is epoxied to the plastic which is epoxied to the front Ti "L".

3.3 Systematic Errors

Systematic errors are errors which are associated with the direction of the electric field, and as such cannot be averaged out by repeated measurements. The sensitivity of the experiment will be limited by these errors if not kept below the projected sensitivity. Using cold trapped atoms decreases some systematic errors such as $\mathbf{v} \times \mathbf{E}$ effects that were substantial in previous beam-based experiments. However, there are new systematic errors which relate directly to using cold trapped atoms. In this section potential systematic errors that result from magnetic field gradients are discussed. These errors include electric field gradients and imperfect electric field reversal.

A spatially inhomogeneous electric field can be the result of non-parallel or not-flat electric field plates. Discharges from one plate to another can cause damage and lead to localized non-conductive spots near certain groups of atoms. The displacement from

an electric field gradient of 100 V/cm^2 is about 0.01 mm [14]. The magnetic field between the groups cannot change by more than 0.14 pG for Cs which means the magnetic field gradients need to be controlled to less than 140 pG/cm.

Chapter 4

Magnetic Fields

As seen in Chapter 3, the EDM experiment is sensitive to magnetic fields under certain conditions. In this chapter, sources of stray magnetic fields and methods for controlling the magnetic fields are discussed. These methods include, from the outermost to innermost: 3 sets of Helmholtz-like coils, μ-metal shields, and finally 8 sets of magnetic field coils.

4.1 Sources of Stray Magnetic Fields

The magnetic field and magnetic field gradients in the lab were measured using magnetic field sensors. In the measurement region the magnetic field is on the order of hundreds of mG [14]. There is also 60 Hz noise on the order of hundreds of μG and gradient field fluctuations on the order of 10 μG/cm/$\sqrt{Hz}$ [14].

4.2 Outer Magnetic Field Coils

Outside the magnetic shields there are 3 sets of Helmholtz-like coils which cancel the bias magnetic fields inside the measurement region (with no shield present) to the order of mG. The main purpose of these coils is to ensure that the μ-metal shields are not saturated, so that the maximum shielding factor can be obtained.

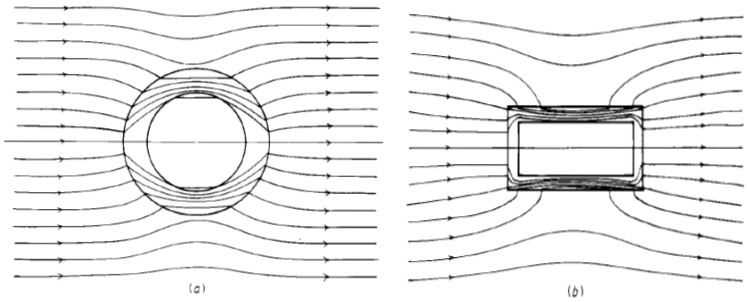

Fig. 4.1. Illustration of magnetic flux through a high μ magnetic shield in (a) the transverse direction and (b) the axial direction, from reference [30].

4.3 μ-Metal Shields

Ferromagnetic materials with a high magnetic permeability, μ, can be used to "collect" the magnetic field flux away from the shielded region (see Figure 4.1). The effectiveness of the magnetic shield is determined by its shielding factor, which is defined as $S = \frac{B_{shielded}}{B_{unshielded}}$. With the current design a shielding factor of 57000 is expected, although this result is fairly uncertain. It is important to note that this is the level of shielding from the field outside the measurement region. The field inside the measurement region will most likely be dominated by the magnetic fields produced by the μ-metal itself.

4.4 Inner Magnetic Field Coils

Inside the μ-metal shields magnetic fields on the order of μG are still expected. In order to control these magnetic fields 8 sets of magnetic field coils are used to cancel the 3 bias fields (B_x,B_y,B_z), the 3 gradient fields ($\frac{dB_x}{dx}$,$\frac{dB_y}{dy}$,$\frac{dB_z}{dz}$), and 2 independent cross derivative fields ($\frac{dB_x}{dz}$,$\frac{dB_z}{dy}$). The magnetic field derivative terms will need to be canceled

as well as possible, but the bias fields will be necessary to scan the magnetic field to map the Ramsey fringe.

The ideal cylindrical sheet currents for the coils can be obtained from the boundary condition (ignoring proportionality constants) $\mathbf{n} \times \mathbf{H} = \mathbf{K}$, where the field we wish to create is $\mathbf{H}$, $\mathbf{n}$ is the normal vector to the cylindrical surface, and $\mathbf{K}$ is the surface current. The surface currents obtained from this equation are shown in Figure 4.2, for simplicity the 3 surface currents involving y are not shown since they are symmetric to x in a cylindrical coordinate system. The coils are made of 2 mil copper foil wrapped

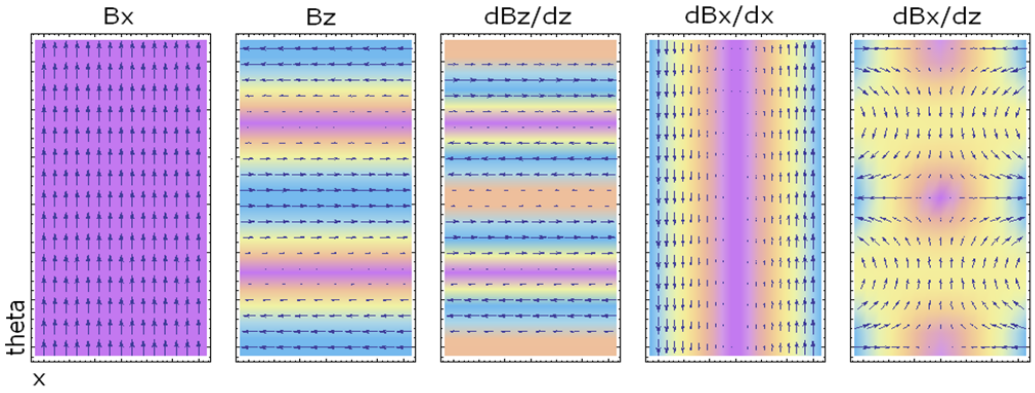

Fig. 4.2. Ideal surface currents for a cylindrical sheet for the fields shown. Since the cylinder is symmetric about the z axis the B_y, $\frac{dB_y}{dy}$, and $\frac{dB_y}{dz}$ configurations can be obtained from the associated x sheet currents.

around the plastic chamber containing the cavity optics. The magnetic field produced by the $\frac{dB_z}{dz}$ coils is given by Equation 4.1.

$$\frac{dB_z}{dz}(I) = I \times 0.039(G/cm)/A. \tag{4.1}$$

Since $\frac{dB_z}{dz}$ is the field the experiment is most sensitive to, this calibration will be used in Section 4.5, where the current source for the coils is discussed.

4.5 Inner Magnetic Field Current Source

To produce a magnetic field the inner magnetic field coils must have an 8-channel, stable, low-noise current source that can be automatically updated from a control program. This current source must meet a number of high performance requirements (assuming the magnetic field calibration given by Equation 4.1), including:

- current fluctuations less than 0.4 nA/$\sqrt{Hz}$
- accurate to approximately 700 pA, including any thermal drifts
- a maximum current of at least 20 μA

In order to achieve this level of precision a 16-bit voltage output digital to analog converter (DAC) and operational amplifier (op-amp) will be used as a transimpedance source. A large resistor (100 kΩ) with a low temperature coefficient of resistance (TCR) will be placed in series with the coils to convert the stable voltage to a stable current. This has the benefit that the current is insensitive to the resistance of the coils, which may not have a stable resistance. This current source will be discussed in detail in Chapter 5.

Chapter 5

Current Source Design

In this chapter the proposed design for an 8-channel, 16-bit, low-noise, stable current source is described, and a single channel prototype is tested. This device will be used to drive a current through a set of copper coils designed to control the magnetic field to the first derivative inside a μ-metal magnetic shield described in Section 4.3. Possible sources of error and noise associated with the current source will be considered. Experimental verification of the specifications mentioned here is discussed in Chapter 6.

5.1 Error Budget

The experiment is sensitive to the types of errors which could produce an EDM signal discussed in Section 3.3. For example, a magnetic field gradient in combination with an electric field gradient and an imperfect electric field reversal could cause an EDM signal. It has been determined that a reasonable estimate to stay within the projected sensitivity, is that the resolution of the $\frac{\partial B_z}{\partial z}$ gradient coil needs to be 100 pG/cm (Section 3.3). The current source will be designed so that the resulting magnetic field is accurate to 15 pG/cm. This implies a magnetic field precision of 30pG/cm or smaller, or a current precision of about 700pA for Cs or a voltage precision of 70 μV, with a 100 kΩ resistor.

5.2 Noise Budget

In the ideal case the magnetic field noise should contribute less than the shot noise limit of the experiment. Using preliminary estimates for the ratio of current through the coils to the magnetic field produced, the maximum voltage noise can be determined. Because the experiment is most sensitive to fluctuations in the $\frac{dB_z}{dz}$ gradient coil, the estimated calibration for this coil of 0.039(G/cm)/A will be used. A maximum current noise of 0.4 nA/$\sqrt{Hz}$ implies a maximum voltage noise of 40 μV/$\sqrt{Hz}$, with a 100 kΩ resistor.

5.3 Circuit Design

The circuit design centers around a voltage output digital to analog converter (DAC) that receives serial data from a control program. Figure 5.1 is a simplified schematic of the design[1]. The Analog Devices DAC, AD5542C, was selected since it has a voltage resolution of 31.2 μV with a 2.048V reference and the potential to operate in either bipolar or unipolar output modes [31]. Bipolar operation would sacrifice the LSB of precision and the resolution would be 62.4 μV.

Since the magnetic bias coils are also needed for low-frequency magnetic field transitions the 3 bias coil current sources will actually have two current sources associated with each coil. The first current source will be similar to the circuit described here, the second current source will be a separate device capable of producing higher magnitude

[1] see Figure A.1 for the complete design and parts list

and non-constant magnetic fields. Care will be taken in the design so that the effect of the high frequency source on the DC source will be negligible.

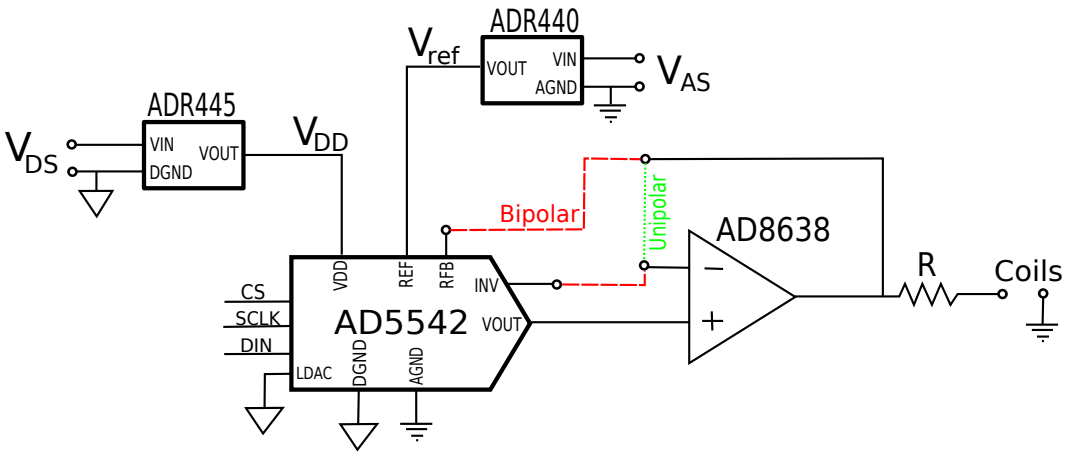

Fig. 5.1. A simple schematic of the current source for gradient coils, for the full schematic see Figure A.1. The green connection will be made when unipolar output is desired. The red connection will be made when bipolar output is desired. V_{ref} is the analog voltage reference output, V_{AS} is the analog supply voltage, V_{DD} is the digital voltage reference output, and V_{DS} is the digital supply voltage. Notice the digital and analog sides are isolated, this is demonstrated in the figure with separate symbols for DGND and AGND.

5.3.1 Components

The DAC is essentially an R2R ladder, See Figure 5.2. The name R2R ladder comes from the values of the resistors used, a resistor of value R is paired with a resistor of value 2R. This specific ratio allows the nodes between the R resistors to take on half the voltage of the previous node. The voltage is then applied across the 2R resistor after which a switch either directs the current through the load or directly to ground. One benefit to this design is that the output impedance of the DAC is not dependent on the

orientation of the internal switches. The total output voltage is given by Equation 5.1.

$$V(N) = \frac{N}{2^{16}} V_{ref}. \tag{5.1}$$

Here N is the integer decimal input (0 to $2^{16} - 1$, and V_{ref} is the analog voltage reference. Equation 5.1 is an idealized case of what is referred to as the "DAC transfer function". The DAC transfer function which will be used in this discussion is determined experimentally as the linear fit to the output current.

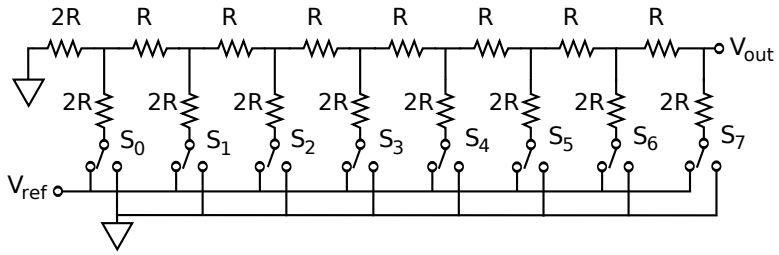

Fig. 5.2. A simple 8-bit R2R ladder. The orientation of the switches (S_0 - S_7) determine the output voltage of the ladder.

In reality the design of the DAC splits the 4 MSBs of the normal R2R ladder, in Figure 5.2, into 15 switches. The 12 LSBs are operated in the normal way, see Figure 5.3.

The DAC requires a reference voltage, V_{ref}, between 2 and 5 V, which determines the output range of the DAC as seen in Equation 5.1. The design uses an ADR440B 2.048V voltage reference that will be referred to as the analog voltage reference. Additionally, the DAC requires a 5V digital power supply, that is isolated from the analog voltage. The digital power supply is be provided by an ADR445A 5V voltage reference.

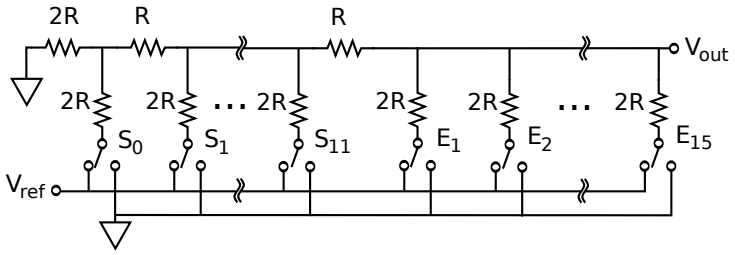

Fig. 5.3. The actual circuit diagram for the DAC. The 4 MSBs are decoded into the 15 switches (E_1-E_{15})

The analog voltage reference is powered by a 6 V battery to minimize noise. The digital voltage reference will either be powered by a separate battery or by an AC/DC converter. Whether there is sufficient isolation from the digital supply to the voltage output to use an AC/DC converter will be determined experimentally.

The op-amp is an AD8638 auto-zero amplifier in a non-inverting orientation. It acts as a buffer between the output and the DAC. The device was chosen for its low-noise, extremely low voltage offset, and small voltage offset drift. The op-amp will be operated in the dual-supply mode and the positive supply voltage will be supplied by the same 6 V battery that powers the analog voltage reference. The negative supply will be powered by a separate 6 V battery of the same type.

5.4 Sources of Errors

The total error must be kept below 70 μV. In this section possible sources of error are modeled as static errors and drift errors associated with changes in temperature or supply voltage.

5.4.1 Static Errors

Static errors ideally should be kept less than the 70 μV goal. However if these errors are found to be larger than the minimum allowable error, corrections could be applied to the DAC transfer function to meet the specifications.

The DAC has a range of error specifications associated with it, that are defined here. The relative accuracy or integral nonlinearity (INL) is defined as the maximum deviation from the DAC transfer function. The differential nonlinearity (DNL) is the difference between the actual change and the ideal change (1 LSB) between two consecutive input codes. The gain error (GE) is the deviation in the slope of the DAC transfer function from the ideal (V_{ref}). The zero code error (ZCE) is the actual output when an input of $N = 0$ is sent to the DAC. The DAC transfer function with these errors included is given by Equation 5.2.

$$V(N) = \frac{N}{2^{16}}(V_{ref} + V_{GE}) + V_{ZCE} + V_{INL}(N) \tag{5.2}$$

V_{GE} and V_{ZCE} can be accounted for empirically. Tests will be done to see whether V_{INL} is constant or not.

A form of INL error is a "Bit flip" error. Bit flip errors are a consequence of the R2R ladder design. If a considerable amount of the least significant switches have a reasonably sized error, then when all these switches are on the errors can sum to an error which is no longer within the acceptable range. This becomes apparent when looking at consecutive values and there is a large change in the INL linearity between two numbers. These errors are easiest to spot in a binary representation of the inputs. In binary, each

digit corresponds to the state of the switch in the R2R ladder. For example, $N = 4095$ is 0000111111111111 in binary, and the left-most and right most digits correspond to the state of the MSB and the LSB respectively, where "0" means the switch does not contribute any current to the output and "1" means that the current controlled by the switch is added to the output. If each of the 12 least significant switches controlled a current which had an error on the order of 0.1 LSB then when all these switches were "on" the error could be as large as 1.2 LSB which could be large compared to the next digit $N = 4096$ (0001000000000000) and an abrupt change in the INL could be observed at this transition. This is referred to as a bit flip error in the 4th MSB.

5.4.2 Drift Errors

Unlike the static errors described in Section 5.4.1, drift errors can not be corrected for by modification of the DAC transfer function. Instead certain operating conditions must be imposed so that errors associated with thermal or supply voltage drifts are always in the allowable range when the conditions are met.

Temperature fluctuations of the current source have the potential to cause significant problems as temperature drifts of 0.5°C are not uncommon in the lab. All electrical components have some form of temperature dependence, and the implications of each component's temperature dependence on the output will be discussed here and listed in Table 5.1. The analog voltage reference has a temperature drift of 3 ppm/°C over the range −40°C to 125°C [32]. The LSB of the design is $1/2^{16}$ or about 15 ppm of the MSB. This implies a voltage drift of less than 0.2 LSB/°C. The absolute Temperature Coefficient of Resistance (TCR) for the load resistor is 0.2 ppm/°C [33]. Therefore an

error of 0.013 LSB/°C is expected. The op-amp has an offset voltage drift of 0.06 μV/°C, or equivalently 0.002 LSB/°C [34]. There is also a drift associated with the gain error and the zero code error of the DAC. The zero code error has a drift of 0.004 LSB/°C and the gain error temperature drift is 0.007 LSB/°C [31]. Therefore the temperature drift is dominated by the voltage reference, which in order for the output to change by the LSB the temperature must change by at least 5 °C. It is straightforward to maintain the temperature within this range. A thermistor will be implemented to monitor the temperature of the device. Measures may be needed to maintain temperature stability including minimizing air currents, actively controlling the temperature with a Peltier cooler, or maintaining the device at a constant, slightly elevated, temperature.

Component	Temp Drift (ppm/C)	Temp Drift (LSB/C)
ADR440B	3	0.2
Load Resistor	0.2	0.013
Op-Amp	0.02	0.0013
DAC (GE)	0.1	0.007
DAC (ZCE)	0.05	0.004

Table 5.1. Temperature drifts of the current source components

Changes in supply voltages for the voltage reference, op-amp, and DAC could result in changes in the output of these devices. The attenuation of the supply voltage for the voltage reference is $\Delta V_{ref}/\Delta V_s = 5 \times 10^{-5}$, or 50 ppm [32]. Therefore for a voltage error on the order of the LSB the supply voltage would have to change by 10% or 0.6 V. The time required to discharge the 6 V batteries to this voltage drawing a mA current is not given on the datasheet, and will have to be determined experimentally. However when drawing a current of 3.6 A a discharge voltage of 5.25V is reached in about

10 hours [35]. This suggests that it will most likely take a few days to discharge enough to reach an error on the order of the LSB. The op-amp has a power supply rejection ratio of 114 dB which is insignificant compared to the voltage reference [34]. The power supply rejection ratio for the DAC is a change in the output of the LSB when the digital supply, V_{DD}, changes by 10%, or 0.5 V [32]. Since the digital supply is controlled by the digital voltage reference V_{DD} will not change by any appreciable amount.

5.4.3 Other Error Sources

There are also two error specifications from changes to the digital input. The first is the digital-to-analog glitch impulse when the DAC changes state, and is measured as the area of the glitch in nV-sec. The second is the digital feed through, which is the measure of the impulse transferred to the analog output when the digital input is changed but the state is not updated. In order to combat this it will be necessary to make sure no digital information is sent to the device during the integration time.

5.5 Sources of Noise

Ideally the total noise should be less than 40 $\mu V/\sqrt{Hz}$, or 86 μV_{rms} for the frequency bandwidth 0.1 to 10 Hz. The noise contributions from each component will be discussed for the frequency bandwidth 0.1 to 10 Hz and summarized in Table 5.2. The DAC has no noise specification listed. The peak-to-peak voltage noise of the analog voltage reference is 1 μV [32]. The op-amp has a peak-to-peak voltage noise of 1.2 μV [34]. The Johnson noise and current shot noise in the 100 kΩ resistor must also be considered. Johnson noise was discussed in Section 3.2.1 in relation to bulk conductors

and magnetic fields, however for a 100 kΩ resistor the RMS voltage noise is 0.13 μV. The current shot noise is the noise associated with the discrete nature of electrons in a current. The shot noise is governed by the Poisson distribution and for the maximum current output of 20 μA the current shot noise is approximately 10 pA.

Component	Peak to Peak Voltage Noise (uVp-p)
ADR440B	1
Load Resistor	0.8
Op-Amp	1.2

Table 5.2. Noise contributions from individual components of the current source for the frequency bandwidth 0.1 to 10 Hz. Conversion from RMS voltage to Peak to Peak voltage defines the peak voltages as 6.18 times the RMS voltage, or 99.9% accuracy.

In order to reduce 60 Hz noise from external sources the current source is placed in a metal box which has been connected to the digital ground (DGND). Grounding the box reduces the pick-up from other sources.

5.6 Data Transfer

To obtain the desired output from the current source, the binary input must be transferred to the DAC. The DAC has a 4 wire serial input consisting of chip select (CS), clock (SCLK), data input (DIN), and execute (LDAC) channels. These can be seen in Figure 5.1. In order to optically isolate the output from noise on the digital input, photoMOS switches are placed between the digital I/O board and the DAC. A pull up or down resistor in combination with a photoMOS switch is used to alternate between the required 0 and 5 V digital input voltages. This setup can be seen in Figure 5.4. Pull up/down resistors have the advantage that an "off" state can be chosen which

draws no current. Since the CS pin must be low during data transfer and high the rest of the time it is advantageous to make the off state of the CS pin high so that it only draws power when data is being transfered. Additionally a large resistor can be used to reduce the current in the "on" state. This helps to extend then life of the battery powering the digital side, but means that the CS pin is inverted from the normal operation.

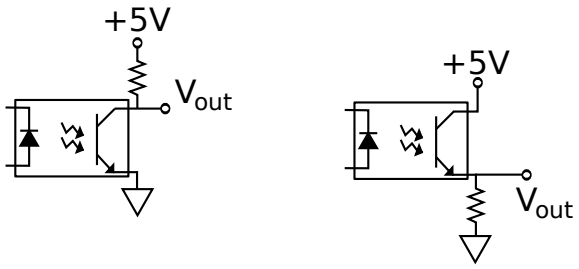

Fig. 5.4. Schematic of a pull up/down resistor

To transfer data to the current source, data is read into the DAC on the rising edge of SCLK. First the CS pin on the DAC must go low, which means that the CS signal out of the control unit must be high because of the inverting configuration. A 16-bit digital word is then fed to the device on the DIN pin starting with the MSB. Finally the CS pin is raised back up (the output from the control unit goes low) and the data is read into the DAC. To make the DAC output the new value the LDAC pin must be low. In this design the LDAC pin is tied to ground so the output is updated when the CS pin is raised. The timing diagram is shown in Figure 5.5. The input voltages are 5 V digital signals which are created temporarily by a National Instruments DAQ, that will later be used to control a direct digital synthesizer board (DDS). The DAQ outputs

an 8-bit digital word which contains the current state of the 3 channels shown in the Timing diagram.

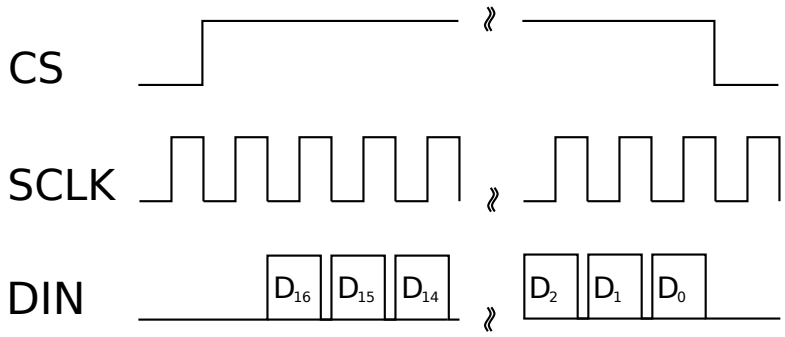

Fig. 5.5. Timing diagram for digital input to the current source. The voltages are D_i is high or low depending on the input value.

In order to address the current source's 8 channels in the final design, a 3-bit decoder will be used to have the desired CS pin go high and all 8 devices will listen on the same DIN line. This method is suggested in the manual and should be fast enough for our purposes [31]. Using optical isolation implies slower rates of data transfer and since at least $16 \times 8 = 128$ bits of data must be transferred in serial, it is conceivable that the rise and fall time of each switch would be long enough that transferring 128 bits would take too long on the timescale of the experiment. In order to combat this the fastest optical switches, that do not require external power, were selected. The photoMOS used is the CPC1560, which uses an external capacitor to reach turn-on and turn-off times of 100 and 400 μs respectively [36]. This implies that the maximum transfer rate is approximately 2 kbps, and all eight DACs might require 64 ms to be updated. These times can be shortened if necessary since the digital high and low on the DAC are 2.4

and 0.8 V respectively, so the rise time to the digital high and the fall time to the digital low could be determined [31]. Currently the device is being used at 8 kbs with no noticeable problems. Another solution is to give each DAC its own micro-controller, then the data could be loaded onto the 8 micro-controllers at a much faster rate, and then all 8 DACs could be updated simultaneously. Finally, if it turns out to be possible to power the digital voltage reference with an AC/DC converter then power consumption of the switches would no longer be a worry and logic output optical isolators, could be used.

5.7 Power Supply

The current source will use PS-6360 6 V 36.0 Ah rechargeable sealed lead acid batteries for power, 2 for the analog and 1 for the digital power supplies. Batteries have much lower noise than an AC/DC converter but the output voltage will drift over time while discharging. When one of the analog batteries loses 10% of it's nomial voltage the analog voltage reference will change its output voltage by the LSB. The exact voltage of the digital battery is not important as long as it is slight above the 5 V minimum for the digital voltage supply.

The batteries were chosen to have such a large capacity to extend the time between charging cycles as much as possible. Each battery will have a duplicate backup battery which can be switched to when the first battery needs to charge, allowing for uninterrupted operation. The battery charger is a PSC-6300A floating charger which will only charge the battery when it is below a certain cut-off voltage insuring maximum standby lifetime. An example circuit for the power supply is shown in Figure 5.6.

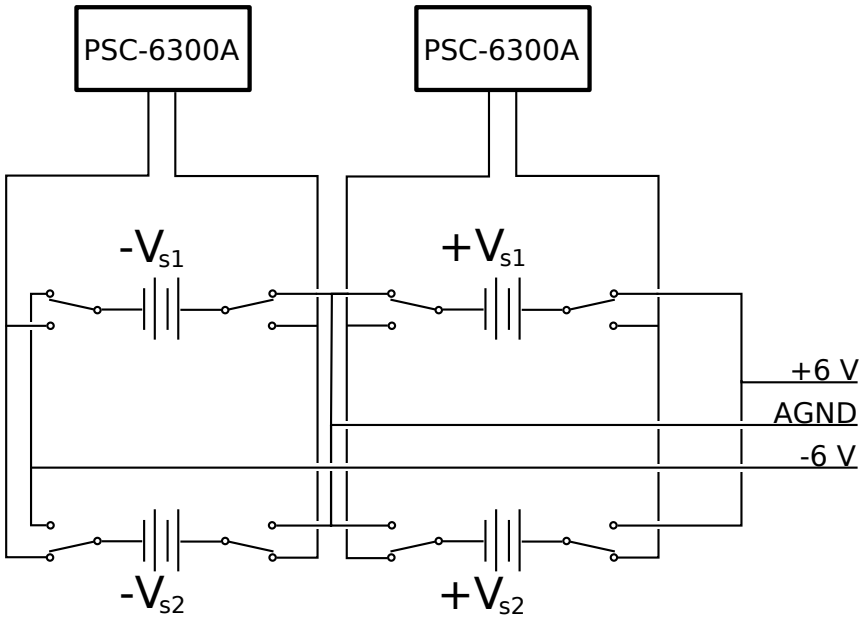

Fig. 5.6. Circuit diagram for the analog battery power supply and recharging system. All the switches will be controlled by one or two mechanical switches for ease of use and to prevent unwanted connections.

Chapter 6

Current Source Tests

In this chapter the errors and noises discussed in Chapter 5 are tested empirically. Tests which have been performed include the integral non-linearity, measurement of long time-scale drifts, and the charge on the batteries over time. The methods of each measurement will also be described in the corresponding sections. Due to a backorder of the low Temperature Coefficient of Resistance (TCR) resistors one of the extra 100 kΩ pull up/down resistors from the digital side of the device is used as the load resistor in the following tests. The TCR of this resistor is 100 ppm/^{0}C which is 2000 times worse than than the low TCR resistor.

6.1 Intergal Non-Linearity

The integral non-linearity is defined as the difference from the actual output of the current source from the output dictated by the DAC transfer function. The DAC transfer funciton is determined experimentally to be the linear fit of the current output to the decimal input. For convenience the difference is scaled relative to the least significant bit (LSB) or 2.048 V/$(100k\Omega \times 2^{16}) = 312.5$ pA.

The INL is measured for decimal inputs, N, in intervals of 200 due to time constraints. The entire process is automated on the control computer and takes about 30 minutes to complete. First the picoammeter (Keithley Model 6485 Picoammeter) is reset

and a reading is taken with no current on the input. This reading is used to zero the picoammeter. A measurement is taken at an input value by first sending the desired value to the current source as described in Section 5.6. The output is then measured 20 times and stored in the picoammeter until the measurement cycle is over. The 20 data points are converted into a average and standard deviation. The standard deviation is usually less than 50 pA or 2 pG/cm, a histogram for a decimal input $N = 6000$ with 2000 data points is shown in Figure 6.1. Then the next point in the series is measured. The zeroing procedure is performed when the decimal input is a multiple of 10,000 to account for drifts in the ammeter.

The INL is shown in Figure 6.2. The DAC transfer function can be obtained from the linear fit of this measurement and is given by Equation 6.1.

$$I_{out}(N) = N \times 0.315129nA + 0.567nA. \tag{6.1}$$

While not all points are observed, the maximum absolute INL is 3.2 LSB. In other words, the most the output varries from Equation 6.1 is 1.01 nA, or 40 pG/cm.

From Figure 6.2, there are a few places where the INL makes large jumps from one point to the next. At these points it is advantagous to take data for the 200 individual points between the original data points to see how the large change happens. This is shown for N =4000 to 4200 in Figure 6.3. The INL changes by 2.09 LSB from $N = 4095$ to 4096. This is an example of a "bit flip" error, which are described in Section 5.4.1. The 4th MSB bit flip can be observed with 8 different orientations of the 3 MSBs. These are shown in Table 6.1.

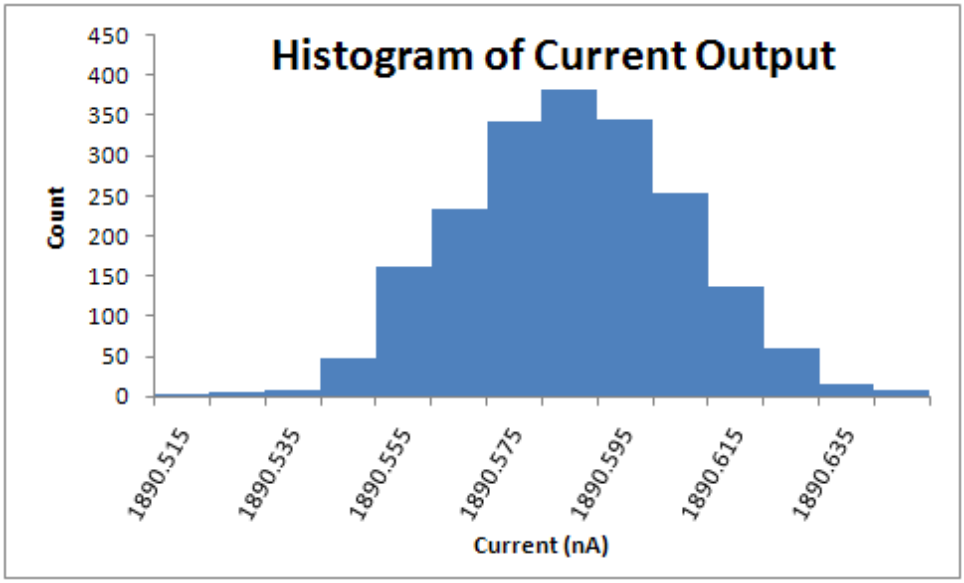

Fig. 6.1. Histogram for N = 6000

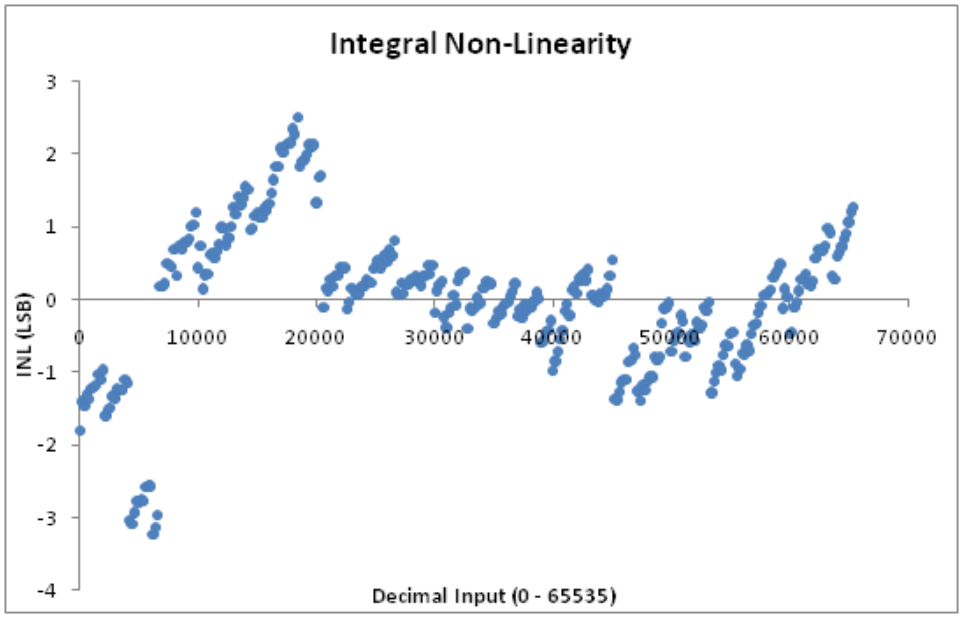

Fig. 6.2. Integral non-linearity of the current output from the DAC scaled to the LSB. The decimal inputs are multiples of N = 200.

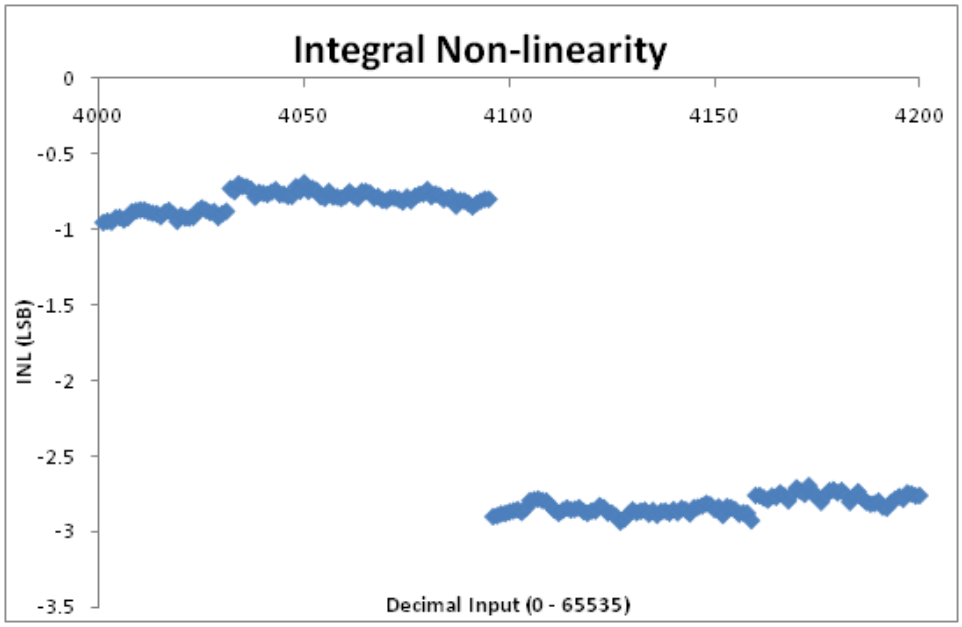

Fig. 6.3. Integral non-linearity of the current output from the DAC scaled to the LSB. Decimal inputs are all integers from N = 4000 to 4200.

Decimal Input	Binary Input	INL (LSB)	Change in INL (LSB)
4095	0000111111111111	-0.80	
4096	0001000000000000	-2.90	-2.09
12287	0010111111111111	1.18	
12288	0011000000000000	0.93	-0.25
20479	0100111111111111	1.94	
20480	0101000000000000	-0.03	-1.97
28671	0110111111111111	0.36	
28672	0111000000000000	0.002	-0.37
36863	1000111111111111	-0.36	
36864	1001000000000000	-0.92	-0.56
45055	1010111111111111	0.23	
45056	1011000000000000	-1.90	-2.13
53247	1100111111111111	-0.15	
53248	1101000000000000	-1.60	-1.45
61439	1110111111111111	-0.02	
61440	1111000000000000	-0.66	-0.63

Table 6.1. Table of all 8 4th MSB bit flips

These bit flip errors can be observed at other switches and can also be seen in Figure 6.3 at 4031 (0000111110111111) to 4032 (0000111111000000) and the bit flip 4159 (0001000000111111) to 4160 (0001000001000000). Both of these errors are a bit flip in the 7th LSB (64) of 0.15 and 0.166 LSB respectively.

6.2 Long Time-Scale Drifts

Long time-scale drifts in the output current are measured using the picoammeter and taking a single measurement triggered at a desired interval for 2000 data points. The temperature inside the box is measured at 2 minute intervals. Since the low TCR resistor is backordered the data presented in this section should act as an upperbound on the actual temperature drift error. Current output data taken at 23 second intervals is shown in Figure 6.2. The peak-to-peak variation of the current over the 12.8 hour measurement is 153 pA and the peak-to-peak temperature variation is 0.14 ^{o}C. The supply voltage change is bounded above by 10 mV because of the accuracy of the multimeter used to take measurements.

6.3 Low-Frequency Voltage Noise

Low-frequency voltage noise has not yet been measured. The noise will determined by connecting the low-frequency spectrum analyzer across the output of the current source with no load attached. The voltage noise will measured over the frequency bandwidths 0.1 to 10 Hz and 10 to 100 Hz.

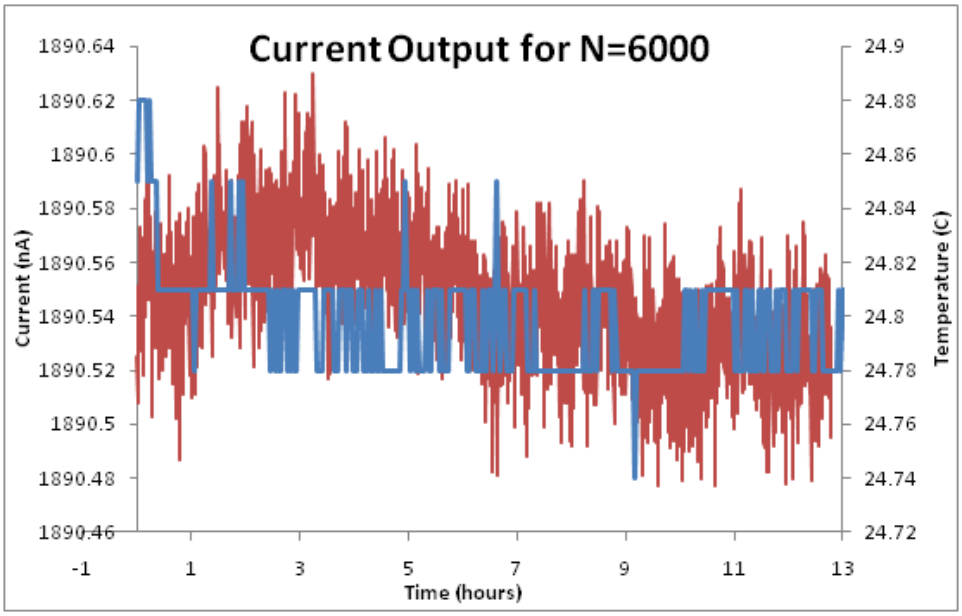

Fig. 6.4. Current output for N=6000 is sampled every 23 seconds for 12.8 hours. The temperature is sampled every 2 minutes.

6.4 Battery Discharge Rate

The battery charge has been monitored over two weeks while constantly drawing a current and is shown in Figure 6.5. More time is required to determine how long it would take for the voltage to drop to 10%. The final current source will draw 8 times the current than the prototype which is tested here.

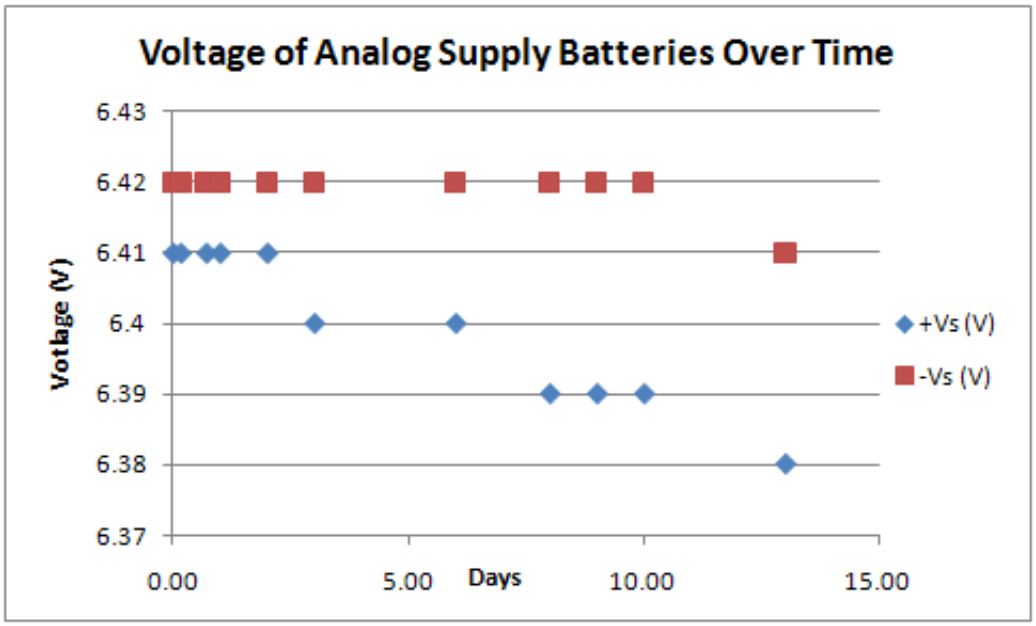

Fig. 6.5. The discharge rate of the ±6 V analog supply batteries over two weeks

Chapter 7

Conclusion and Future Work

7.1 Conclusion

A broad overview of an experiment to search for the electric dipole moment (EDM) of the electron has been given. The measurement will be done with cold trapped Cesium and Rubidium atoms in 2 1D optical lattices separated by 1 cm in alternating measurements. A sensitivity of 3×10^{-30} e-cm is anticipated with a 3 second coherent evolution in a 150 kV/cm electric field and an integration time of 12 hours.

In this thesis, the design for a current source for inner magnetic field coils is presented and tested experimentally. With no error correction the unipolar current source is accurate to within 1.01 nA or 40 pG/cm. An accuracy on the order of 100 pG/cm is required, see Section 3.3. A first-order error correction could be implemented to increase the accuracy further, if necessary. Temperature and supply voltage dependence of the output needs to be characterized, but the low TCR (0.2 ppm/^{o}C) resistor necessary for the tests is on backorder. Instead a resistor with a TCR of 100 ppm/^{o}C was used to take the data so far. With this resistor, the peak-to-peak output for $N = 6000$ of the current source changes by 153 pA or 6 pG/cm over a 12.8 hour period where the peak-to-peak temperature change was 0.14 ^{o}C. The supply voltages were not observed to change over the measurement period, and the multimeter for the measurement has a precision of 10 mV.

7.2 Future Work

The prototype for the current source must be tested for temperature and supply voltage drifts with the low TCR resistor. The noise of the output must also be determined using a spectrum analyzer. All specifications must also be checked for the bipolar output as well.

A final design for the 8-channel current source needs to be completed. Certain information is required from the prototype before the final design can be completed. For example the enclosure can either be connected to the digital or analog ground and the optimal choice needs to be determined empirically. Also either the digital or analog ground can be connected to Earth ground. The discharge rate of the supply voltage batteries need to be determined and an enclosure for them, that makes the recharging process simple, must be created. Finally, a program must be created which allows the current source to be controlled by the Supertime program that controls the experiment.

Bibliography

[1] E. M. Purcell and N. F. Ramsey. On the possibility of electric dipole moments for elementary particles and nuclei. *Phys. Rev.*, 78(6):807, Jun 1950.

[2] J. H. Smith, E. M. Purcell, and N. F. Ramsey. Experimental limit to the electric dipole moment of the neutron. *Phys. Rev.*, 108(1):120–122, Oct 1957.

[3] L. R. Hunter. Tests of time-reversal invariance in atoms, molecules, and the neutron. *Science*, 252(5002):73–79, Apr 1991.

[4] Werner Bernreuther and Mahiko Suzuki. The electric dipole moment of the electron. *Rev. Mod. Phys.*, 63(2):313–340, Apr 1991.

[5] I. B. Khriplovich. *CP Violation Without Strangeness: Electric Dipole Moments of Particles, Atoms, and Molecules.* Springer-Verlag, 1997.

[6] T. D. Lee and C. N. Yang. Question of parity conservation in weak interactions. *Phys. Rev.*, 104(1):254–258, Oct 1956.

[7] C. S. Wu, E. Ambler, R. W. Hayward, D. D. Hoppes, and R. P. Hudson. Experimental test of parity conservation in beta decay. *Phys. Rev.*, 105(4):1413–1415, Feb 1957.

[8] Donald H. Perkins. *Introduction to High Energy Physics.* Cambidge University Press, 4th edition, 2000.

[9] J. H. Christenson, J. W. Cronin, V. L. Fitch, and R. Turlay. Evidence for the 2π decay of the $k2$ meson. *Phys. Rev. Lett.*, 13(4):138–140, Jul 1964.

[10] M. E. Pospelov and I. B. Khriplovich. Electric dipole moment of the w boson and the electron in the kobayashi-maskawa model. *Sov. J. Nucl. Phys.*, 53:638–640, 1991.

[11] B. C. Regan, Eugene D. Commins, Christian J. Schmidt, and David DeMille. New limit on the electron electric dipole moment. *Phys. Rev. Lett.*, 88(7):071805, Feb 2002.

[12] Stephen Barr Norval Fortson, Patrick Sandars. The search for a permanent electric dipole moment. *Physics Today*, 56(6):33–39, Jun 2003.

[13] L. I. Schiff. Measurability of nuclear electric dipole moments. *Phys. Rev.*, 132(5):2194–2200, Dec 1963.

[14] Fang Fang. *Progress Towards a Measurement of the Electron Electrical Dipole Moment Using Ultra-Cold Atoms.* PhD thesis, The Pennsylvania State University, Dec 2007.

[15] D. DeMille, F. Bay, S. Bickman, D. Kawall, D. Krause, S. E. Maxwell, and L. R. Hunter. Investigation of pbo as a system for measuring the electric dipole moment of the electron. *Phys. Rev. A*, 61(5):052507, Apr 2000.

[16] H. S. Nataraj, B. K. Sahoo, B. P. Das, and D. Mukherjee. Intrinsic electric dipole moments of paramagnetic atoms: Rubidium and cesium. *Phys. Rev. Lett.*, 101(3):033002, Jul 2008.

[17] A.C. Hartely, E. Lindroth, and A.M. Martensson-Pendrill. Parity non-conservation and electric dipole moments in caesium and thallium. *J. Phys. B*, 23(19):3417, Oct 1990.

[18] P. G. Harris, C. A. Baker, K. Green, P. Iaydjiev, S. Ivanov, D. J. R. May, J. M. Pendlebury, D. Shiers, K. F. Smith, M. van der Grinten, and P. Geltenbort. New experimental limit on the electric dipole moment of the neutron. *Phys. Rev. Lett.*, 82(5):904–907, Feb 1999.

[19] C. A. Baker, D. D. Doyle, P. Geltenbort, K. Green, M. G. D. van der Grinten, P. G. Harris, P. Iaydjiev, S. N. Ivanov, D. J. R. May, J. M. Pendlebury, J. D. Richardson, D. Shiers, and K. F. Smith. Improved experimental limit on the electric dipole moment of the neutron. *Phys. Rev. Lett.*, 97(13):131801, Sep 2006.

[20] W. C. Griffith, M. D. Swallows, T. H. Loftus, M. V. Romalis, B. R. Heckel, and E. N. Fortson. Improved limit on the permanent electric dipole moment of $hg199$. *Phys. Rev. Lett.*, 102(10):101601, Mar 2009.

[21] N. D. Scielzo, I. Ahmad, K. Bailey, D. L. Bowers, J. R. Guest, R. J. Holt, Z.-T. Lu, T. P. O'Connor, D. H. Potterveld, and E. C. Schulte. Progress towards laser trapping of ra for an electric dipole moment measurement. volume 842, pages 787–789. AIP, 2006.

[22] M. V. Romalis, W. C. Griffith, J. P. Jacobs, and E. N. Fortson. New limit on the permanent electric dipole moment of $199hg$. *Phys. Rev. Lett.*, 86(12):2505–2508, Mar 2001.

[23] J. J. Hudson, B. E. Sauer, M. R. Tarbutt, and E. A. Hinds. Measurement of the electron electric dipole moment using ybf molecules. *Phys. Rev. Lett.*, 89(2):023003, Jun 2002.

[24] F. L. Shapiro. Electric Dipole Moments of Elementary Particles. *Soviet Physics Uspekhi-USSR*, 11(3):345, 1968.

[25] B. V. Vasiliev and E. V. Kolycheva. Measurement of Electron Electric-Dipole Moment Using Quantum Interferrometer. *Zhurnal Eksperimentalnoi I Teoreticheskoi Fiziki*, 74(2):466–471, 1978.

[26] S. A. Kuenzi, O. P. Sushkov, V. A. Dzuba, and J. M. Cadogan. Search for violation of fundamental time-reversal and space-reflection symmetries in solid-state experiments. *Phys. Rev. A*, 66(3):032111, Sep 2002.

[27] E. L. Raab, M. Prentiss, Alex Cable, Steven Chu, and D. E. Pritchard. Trapping of neutral sodium atoms with radiation pressure. *Phys. Rev. Lett.*, 59(23):2631–2634, Dec 1987.

[28] Fang Fang and David S. Weiss. Resonator-enhanced optical guiding and trapping of cs atoms. *Opt. Lett.*, 34(2):169, Jan 2009.

[29] S. K. Lamoreaux. Feeble magnetic fields generated by thermal charge fluctuations in extended metallic conductors: Implications for electric-dipole moment experiments. *Phys. Rev. A*, 60(2):1717–1720, Aug 1999.

[30] T J Sumner, J M Pendlebury, and K F Smith. Conventional magnetic shielding. *Journal of Physics D: Applied Physics*, 20(9):1095, 1987.

[31] Analog Devices Inc. *5V, Serial-Input, Voltage-Output, 16-Bit DACs AD5541/AD5542*, b edition, 2008.

[32] Analog Devices Inc. *Ultralow Noise, LDO XFET Voltage References with Current Sink and Source, ADR440/ADR441/ADR443/ADR444/ADR445*, c edition, 2008.

[33] Vishay Intertechnology, Inc. *VSMP Series (0805, 1206, 1506, 2010, 2512) (Z-Foil)*, Jul 2008.

[34] Analog Devices Inc. *16 V Auto-Zero, Rail-to-Rail Output Operational Amplifiers, AD8638/AD8639*, e edition, 2009.

[35] *PS-6360 6 Volt 36.0 AH Rechargeable Sealed Lead Acid Battery, organization=Power-Sonic Corp.,*.

[36] Clare Inc. *CPC1560 Solid State Relay with Integrated Current Limit*, 11 2009.

Appendix

Full Current Source Diagram

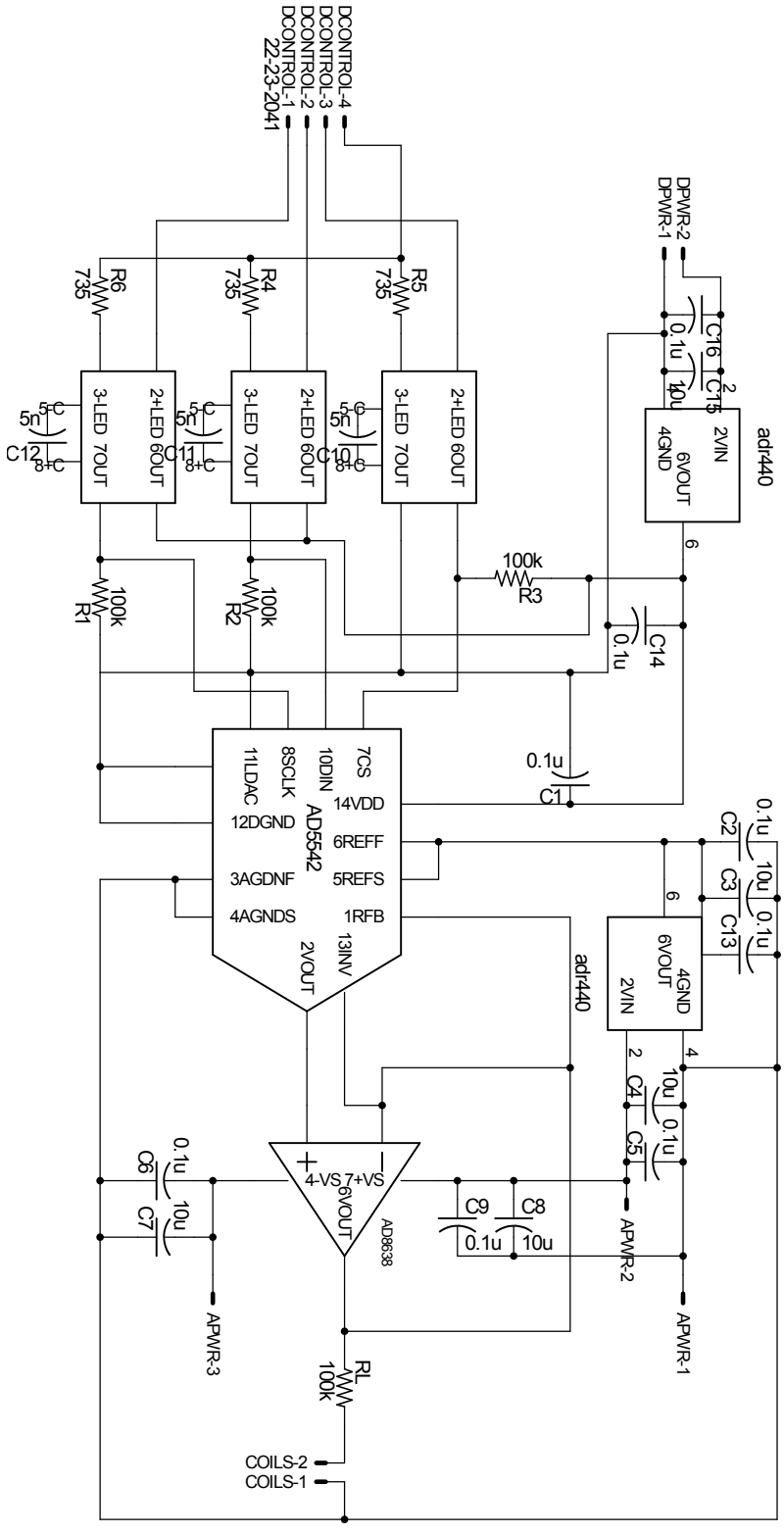

Fig. A.1. Full circuit diagram for single channel prototype current source

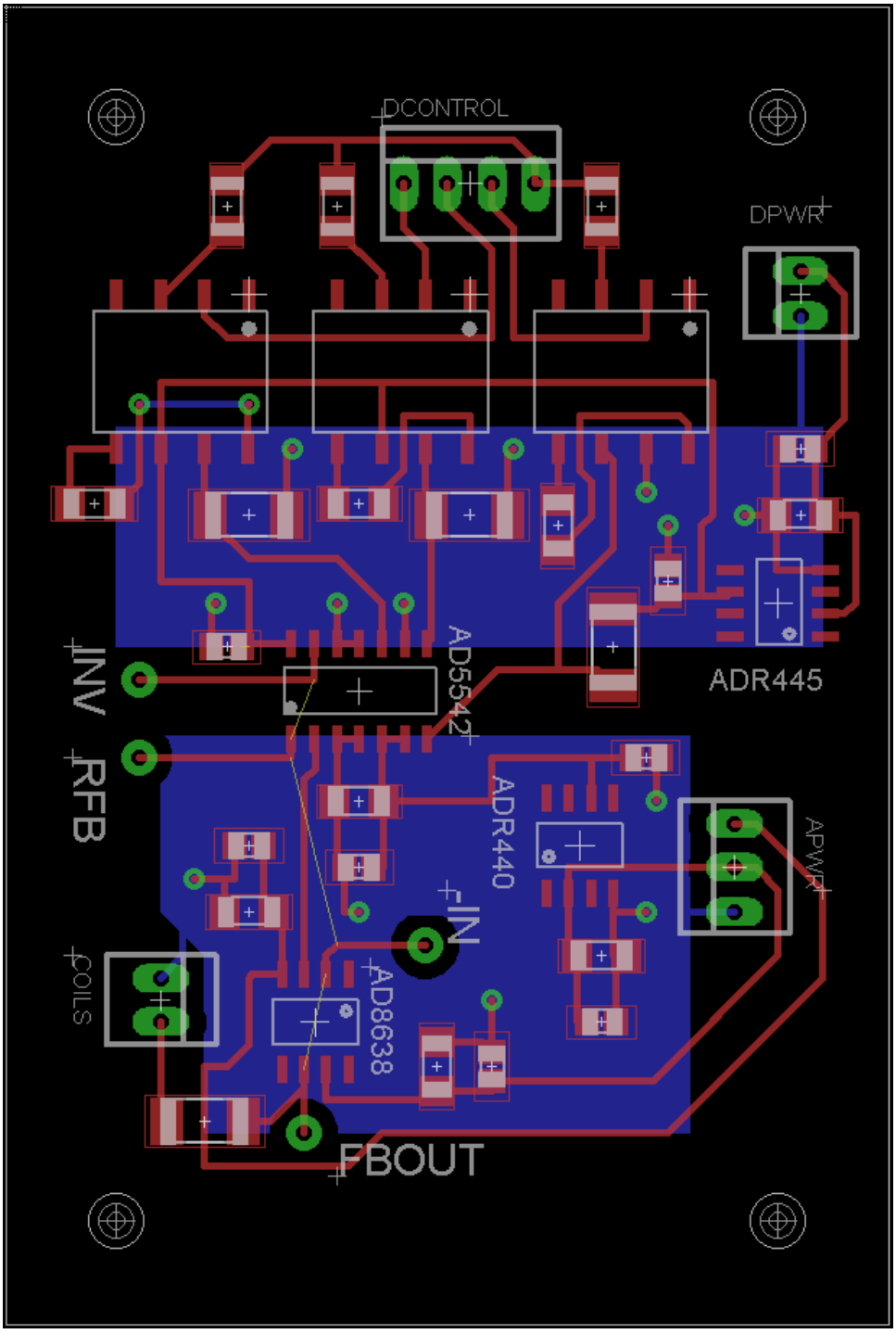

Fig. A.2. Circuit board design for single channel prototype of the current source. Red is the top side of the board, blue is the bottom side, and green is the vias (electrical connections from top to bottom). The yellow wires represent wired connections for switching between bipolar and unipolar output. The board dimensions are 2×3 inches.

Name	Value	Package	Notes
R1	100k	2010	NORMAL RESISTOR
R2	100k	2010	NORMAL RESISTOR
R3	100k	2010	NORMAL RESISTOR
R4	732	1206	NORMAL RESISTOR
R5	732	1206	NORMAL RESISTOR
R6	732	1206	NORMAL RESISTOR
RL	100k	2010	LOW TCR RESISTOR
C1	0.1u	0805	Ceramic
L.,BMGV C2	0.1u	0805	Ceramic
C3	10u	3216	Tantalum
C4	10u	3216	Tantalum
C5	0.1u	0805	Ceramic
C6	0.1u	0805	Ceramic
C7	10u	3216	Tantalum
C8	10u	3216	Tantalum
C9	0.1u	0805	Ceramic
C10	4.7n	1206	Ceramic
C11	4.7n	1206	Ceramic
C12	4.7n	1206	Ceramic
C13	0.1u	0805	Ceramic
C14	0.1u	0805	Ceramic
C15	10u	3216	Tantalum
C16	0.1u	0805	Ceramic
U1	ADR445		5 V Reference
U2	ADR440		2.048 V Reference
U3	AD8638		Op-Amp
U4	AD5542		DAC
U5	CPC1560		PhotoMOS
U6	CPC1560		PhotoMOS
U7	CPC1560		PhotoMOS

Table A.1. Parts list for single channel prototype current source

Vita

Matthew Ebert
124 N Gill St, Apt 3
State College, PA 16801
mfe5003@gmail.com

Education:

Bachelor of Science Degree in Physics and Mathematics
Penn State University, Spring 2010
Honors in Physics
Thesis Title: "Progress Towards a Measurement of the Electron Electric Dipole Moment using Cold Cs and Rb Atoms in a 1D Optical Trap"
Thesis Supervisor: David S. Weiss

Related Experience:

NIST Summer Undergraduate Research Fellowship
Supervisor: Jeeseong Hwang
Summer 2008

Awards:

Dean's List
Physics Department Scholarship